Accounts

Reflection Spectroscopic Study of Organic Conductors

Kyuya Yakushi

Institute for Molecular Science and Graduate University for Advanced Studies,
Nishigonaka 38, Myodaiji, Okazaki, Aichi, 444-8585

(Received August 9, 2000)

The author reviews the low-energy optical transitions in quasi one- and two-dimensional organic conductors studied by polarized reflection spectroscopy. The characteristic optical properties of organic conductors are the strong anisotropy, electron–electron interaction, and coupling with intra-molecular vibration. The method to extract the transfer integrals in anisotropic tight-binding bands is described for several organic conductors. The correlation effect has a big influence on the line shape of the optical conductivity spectrum in the intra-band transition region. The electron–molecular vibration coupling provides us with rich information on the structural fluctuations and structural changes during the phase transition. The observation of plasmons resulting from the mixing with the transverse excitation is caused by the strong anisotropy in electronic structure.

Since the discovery of the organic metal TTF-TCNQ, reflection spectroscopy has been a powerful method to extract the information of the transfer integral, which is the most basic quantity to describe the band structure. TTF-TCNQ exhibits a Drude-like plasma edge in high-frequency region, although in the far-infrared region it is strongly deviated from the Drude-like reflectivity even above the metal-insulator phase transition temperature, due to the fluctuations of the charge-density-waves (CDW).[1] Owing to the lattice instability (electron–phonon interaction) and/or strong electron-electron interaction, the optical conductivity $\sigma(\omega)$ in the low-frequency region deviates from the Drude model that describes the optical conductivity of typical metals. The application of the band picture to the organic conductors has been doubted before, particularly in quasi-one-dimensional organic metals. The unusual optical conductivity in far-infrared region is not yet solved.[2,3] However, the observation of the magnetoresistance and magnetic susceptibility in quasi-two-dimensional organic conductors proved the applicability of the band picture.[4] In addition, the optical conductivity of the high-energy region can be described by the Drude model. So the transfer integrals can be roughly estimated from the analysis of the reflectivity curve in the mid-infrared and near-infrared regions, which is one of the most reliable methods.

Let us discuss the one-electron band model which describes the weakly interacting system. The bandwidth of an organic conductor is typically less than 1 eV, which is much narrower than that (5—10 eV) of a typical inorganic compound. This narrow bandwidth comes from the charge-transfer interaction which is weaker than a covalent bond or metallic bond. The inter-atomic distance between the nearest-neighbor molecules is typically 3.1—3.6 Å. Due to the weakly overlapped frontier orbital, the tight-binding approximation is usually taken to describe the band structure. In the tight-binding approximation, the kinetic energy term of the Hamiltonian is expressed by the following equation:

$$H = -\sum_{l,l'}\sum_{m,m'} t_{lml'm'} a^{+}_{lm} a_{l'm'}, \qquad (1)$$

where a^{+}_{lm} and $a_{l'm'}$ are the creation and annihilation operators at l-th and l'-th unit cells and m-th and m'-th sites in the unit cell, $t_{lml'm'}$ is the transfer integral between m-th site in the l-th unit cell and m'-th site in the l'-th unit cell. Since the distance between the molecules is far, the transfer integrals of nearest-neighbor molecules are taken into account and other ones are neglected. The estimation of the transfer integral is conducted using the Mulliken approximation as $t_{lml'm'} \propto S_{lml'm'}$, where $S_{lml'm'}$ is the overlap integral of the frontier orbitals between the neighbor molecules. The proportional factor is empirically taken as -10 eV.

If the unit cell involves one molecule, the eigen value of Eq. 1, $E(k)$, has one branch. In this case only the intra-band transition is allowed near the Fermi energy, if the band is partially filled and thus the system is in metallic state. Since no finite excitation energy is required, the intra-band transition exhibits a peak at zero frequency ($\omega = 0$). The intra-band transition is formulated based on the Boltzmann equation, and the complex optical conductivity $\sigma(\omega)$ is expressed by the Drude model. The integrated intensity of this optical transition is given by the square of the plasma frequency ω_p.

Incidentally, the plasma frequency $\hbar\omega_p$ corresponds to the excitation energy of the plasmon, the longitudinal excitation of a metal. The plasmon cannot be observed in an isotropic material using the reflectivity method, but it becomes observable in an anisotropic material as will be shown in section 5. When the unit cell contains two molecules, the energy band $E(k)$ split into two branches. In this case another type of optical transition is allowed. This inter-band transition occurs vertically, in other words, the hole and electron is produced at the same wave vector k. This kind of inter-band transition is calculated using the point charge approximation, in which the point charge in the molecule is represented by the center of a frontier orbital. In this case the intensity is determined by the joint density of state at k and the transition probability at k, both of which depend upon the wave vector k.

When the electron–electron interaction is strong (strong correlation), which is more general in organic conductors, the Hubbard model is adopted to describe the correlated system. The correlation effect gets more obvious in the half-filled band system. The Hubbard Hamiltonian is given by the following equation,

$$H = \sum_{lml'm'} t_{lml'm'} a^{+}_{lm} a_{l'm'} + U \sum_{lm} a^{+}_{lm\uparrow} a_{lm\uparrow} a^{+}_{lm\downarrow} a_{lm\downarrow}, \qquad (2)$$

where U is the on-site Coulomb energy. The on-site Coulomb energy describes the repulsive Coulomb energy between the electrons. In this model, the repulsive force is taken into account within the same molecule, and the inter-molecular Coulomb force is neglected. The introduction of the nearest-neighbor Coulomb force to the Hamiltonian (2) leads to an extended Hubbard model. The Hubbard model for a one-dimensional system with a half-filled band is exactly solved, and a finite U opens a gap at the Fermi level. In this model, the excitation energy to create an electron–hole pair is given by the following equation,[5]

$$E(k_+,k_-)/4t = u - \frac{1}{2} + \int_0^{\infty} \frac{J_1(\omega)}{\omega(1+\exp(2u\omega))} d\omega + \frac{\cos(k_+)+\cos(k_-)}{4} + \int_0^{\infty} \frac{J_1(\omega)\{\cos(\omega\sin(k_+)+\cos(\omega\sin(k_-))\}}{\omega(1+\exp(2u\omega))} d\omega \qquad (3)$$

where k_+ and k_- are the quasi-moments of electron and hole, $u = U/4t$, and $J_i(\omega)$ is the Bessel function of the first kind with order i. As displayed in Fig. 1, $E(k_+,k_-)$ takes a minimum at $k_+ = k_- = \pi$, which corresponds to the absorption edge. The vertical transition ($k_+ = k_-$) spans from $E(\pi,\pi)$ to $E(\pi,\pi)+4t$. The transition probability has not been analytically obtained, so that the analytical solution of the optical spectrum has not been obtained so far. However, the integrated intensity of the optical transition in a half-filled one-dimensional system is solved by Baeriswyl et al.[6] The plasma frequency is given by the following equation,

$$\frac{\varepsilon_0}{Ne^2d^2}\frac{\hbar^2\omega_p^2}{4t} = \int_0^{\infty}\left(\frac{1}{\omega(1+\exp(2u\omega))} + \frac{u}{1+\cos h(2u\omega)}\right) J_0(\omega)J_1(\omega)d\omega \qquad (4)$$

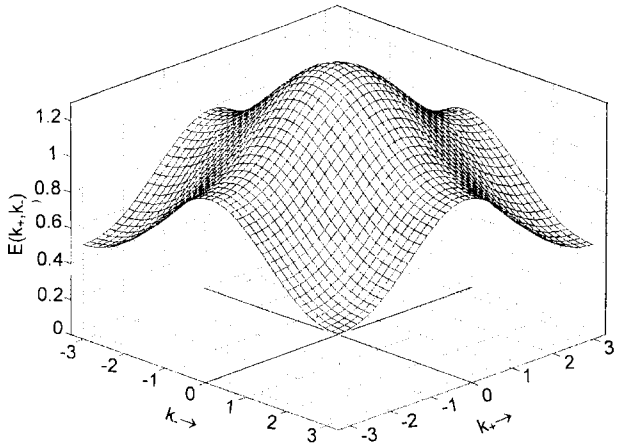

Fig. 1. Excitation energy to produce an electron-hole pair in one-dimensional half-filled Hubbard model.

where N is the density of charge, ε_0 the vacuum dielectric constant, d the inter-molecular spacing between molecules along the chain direction and ω_p the plasma frequency. Combining Eq. 3 with Eq. 4, we can estimate the Hubbard parameter t and U from the analysis of the optical transition. The exact solution has not been given for the optical transition of the quarter-filled band system. A numerical calculation of optical conductivity has been performed for a dimerized quarter-filled band system.[7]

The electron-phonon interaction has an influence on the optical conductivity as well. The effect of the charge-density-wave (CDW) caused by the instability of the quasi-one-dimensional system appears in far-infrared or microwave frequency region. The interaction with totally symmetric molecular vibration influences the optical conductivity in the mid-infrared region. Through this interaction, the molecular vibration induces a large oscillation of electronic density, that is, a big oscillating dipole along the direction of the charge transfer. This is called electron–molecular vibration (emv) coupling. Owing to this oscillating dipole, a strong vibronic band shows up along the conducting direction, usually perpendicular to the molecular plane. At the same time, the frequency of the vibronic mode is very perturbed via this coupling and shows a large low-frequency shift, say, 100 cm^{-1}. The coupling constant of the molecular vibration with the charge-transfer excitation is a fundamental quantity in molecular metals. It contributes to the stabilization of the Peierls state[8] and might be related to the superconducting mechanism[9] as well. The essential point of the emv coupling theory arises from the coupled vibration in a dimer.[10] When the two molecules vibrate in anti-phase, the oscillatory dipole moment is induced along the direction connecting the centers of molecules in the dimer. The emv coupling theory was first formulated on the dimer[10] and then extended to the linear chain system[11]. The conductivity spectrum in the dimer model is formulated as the following equation,[10]

$$\sigma(\omega) = \frac{\omega}{i}\frac{Ne^2d^2}{4}\frac{\chi(\omega)\chi(0)}{\chi(0)-\chi(\omega)D(\omega)} \qquad (5)$$

$$D(\omega) = \sum \frac{\lambda_\alpha \omega_\alpha^2}{\omega_\alpha^2 - \omega^2 - i\omega\gamma_\alpha}$$

$$\chi(\omega) = \frac{2\omega_{CT}|\langle CT|\delta n|G\rangle|^2}{\omega_{CT}^2 - \omega^2 - i\omega\gamma_{CT}}$$

where N is the electron density, d the distance between the center of the molecules in the dimer, λ_α the coupling constant of the α-th phonon, ω_α the unperturbed phonon frequency, ω_{CT} the electronic excitation energy in the dimer, and γ_α and γ_{CT} are the phenomenological linewidth of the phonon and electronic transition. $|\langle CT|\delta n|G\rangle|^2$ is proportional to the transition probability, where $|G\rangle$ and $|CT\rangle$ are the ground and charge-transfer excited states, δn ($= n_1 - n_2$) is the difference of the number operaters. In the dimer model, the out-of-phase molecular vibration couples with the charge-transfer excitation and induces the oscillating polarization in the direction connecting the center of molecules in the dimer. On the other hand, in-phase molecular vibration is decoupled with the charge-transfer excitation. Due to the decoupling, the in-phase mode is detected in Raman spectrum at the same frequency as the free molecule.

In solid state, there are two kinds of excitations: one is the transverse excitation and the other is the longitudinal excitation. The easiest example to understand is the lattice vibration. The deviation from the equilibrium position is polarized perpendicular to the wave vector in the transverse lattice vibration, while the corresponding one is parallel to the wave vector in the longitudinal lattice vibration. In the case of electronic excitation, a transverse excitation always has the corresponding longitudinal excitation in a high-energy region. The well-known example is the plasmon in a metal, which corresponds to the longitudinal excitation of the intra-band transition. Due to the conservation of energy and momentum in the process of optical absorption, the longitudinal excitation cannot be directly detected by the optical absorption or reflection in an isotropic material. In anisotropic materials, however, the frequency dependent dielectric constant is described by three principal values along the principal axes. When the wavevector of light is not parallel to one of these principal axes, the transverse and longitudinal excitations are mixed with each other. Then the mixed excitation is observed in the region between the transverse and longitudinal excitation energies. The electronic absorption band shifts depending upon the angle between the light wavevector and principal axes of dielectric function. This phenomenon is called directional dispersion. The directional dispersion of an exciton of an organic dye has been analyzed by Hesse et al.[12]. The author also found directional dispersion in the exciton absorption of BDNT crystal.[13] In these materials, the angular dependent spectrum is analyzed using the approximation of the uniaxial crystal.

Finally, Fig. 2 shows the organic molecules which appear in this article.

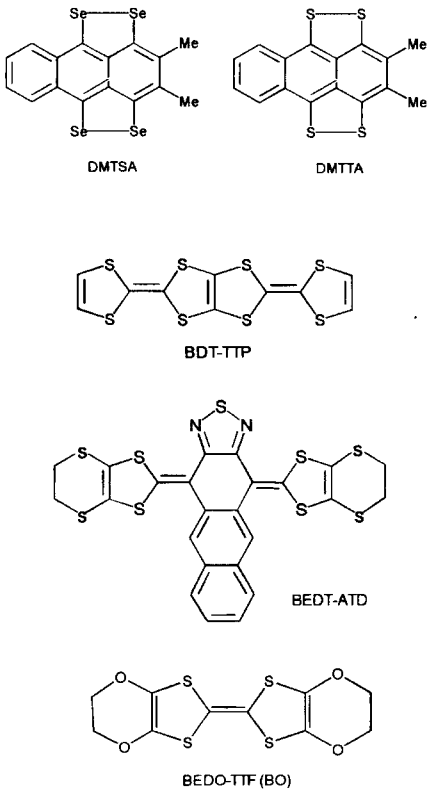

Fig. 2. Molecular structures of electron donors; DMTSA 2,3-dimethyltetraseleno-anthracene, DMTTA 2,3-dimethyltetrathio-anthracene, BDT–TTP 2,5-bis(1,3-dithiol-2-ylidene)-1,3,4,6-tetrathiapentalene, BEDT–ATD 4,11-bis(4,5-ethylenedithio-1,3-dithiol-2-ylidene)-4,11-dihydro-anthra-[2,3-c]thiadiazole, BEDO–TTF (BO) bis(ethylenedioxy)-tetrathiafulvalene.

1. Experimental Setup

The dimension of the single crystal introduced in this article is (0.5—0.2)×(0.2—0.1)×(0.05—0.01) mm^3. To obtain the polarization dependence of single crystals, the spectroscopic measurement is combined with a microscope. The polarized reflection spectrum was obtained with two spectrometers combined with a microscope: FT-IR spectrometer, Nicolet Magna 760, for 600—12000 cm^{-1} region and multi-channel detection system, Atago Macs320, for 11000—30000 cm^{-1} region. The spectra in the region from 600 to 7000 cm^{-1} were collected using a globar light, MCT detector, KBr beam splitter, and wire-grid polarizer; the 4000—10000 cm^{-1} region was measured using a halogen lamp, MCT detector, quartz beam splitter, and Glan–Thompson polarizer; the 8500—12000 cm^{-1} region data were obtained using a halogen lamp, Si photodiode detector, quartz beam splitter, and Glan–Thompson polarizer; the 11000—30000 cm^{-1} region was collected using a xenon lamp, photodiode array system, and Glan–Thompson polarizer. The absolute value of the reflectivity was determined by comparing the reflected light from a gold mirror (600—12000 cm^{-1}) and Si single crystal (11000—30000 cm^{-1}). The single crystal was fixed on a copper sample holder by silicone grease, and the crystal face was adjusted so as to be normal to the incident light by use of a goniometer head. For the low-temperature experiment, a small goniometer head was attached to the cold head of the cryostat Oxford CF1104s, which is fixed on an XYZ stage. The sample on the goniometer head was covered by a radiation shield and a vacuum shroud with a KBr window. The cryostat was evacuated below 10^{-5} Pa by a turbo-molecular pump before cooling the sample. To avoid any contamination on the sample surface at low temperature, the window of the radiation shield was open only for the measurement. The

absolute reflectivity was obtained by comparing the light reflected from a gold mirror placed close to the sample in the cryostat, which could cancel out the spectral dependence of the transmittance of the KBr window. The reflectivity of this inner mirror was monitored at each temperature using the gold mirror outside of the cryostat. The optical conductivity was calculated by the method of modified Kramers–Kronig transformation proposed by Ahrenkiel.[14] The low-frequency side was extrapolated by Hagen-Rubens curve in metallic directions and constant reflectivity in non-metallic direction. The high-frequency side was extrapolated by the constant reflectivity and analytically integrated up to the infinite frequency.

2. Optical Transition in Weakly Interacting Electron System: One-Electron Model

2-1. Quasi-One-Dimensional System: DMTSA-BF_4 in Metallic Phase.[15,16] DMTSA–BF_4 is a molecular metal near room temperature and exhibits a metal-insulator transition around 150 K.[17] As shown in Fig. 3, DMTSA (dimethyltetraseleno–anthracene) is stacked along the c-axis in a zigzag form.[18] The two transfer integrals t_c along the conducting c-axis are equivalent to each other due to the screw-axis symmetry. Due to the zigzag stacking structure, the vector connecting the centers of adjacent molecules has two components, in the c- and b-directions. It is suggested from the polarized reflection spectrum (not shown) that the one-dimensional model along the c-axis is a good approximation. Since the single conducting column in the unit cell contains two DMTSA molecules, the energy band is split into two branches. Owing to the screw-axis symmetry, the two branches stick together at the zone boundary of $k_c = \pi/c$ without opening a gap.[19] The tight-binding band is drawn in Fig. 4 both in reduced and extended schemes. According to the tight-binding approximation, these branches are given by Eq. 6,

$$E^{\pm}(k) = \pm\Delta(k) = \pm t_c\sqrt{2+2\cos(k_c c)}, \tag{6}$$

where t_c is the transfer integral along the c-axis, and+and− represent the upper and lower branches, respectively. Since the highest occupied molecular orbital (HOMO) of $DMTSA^+$ is singly occupied, the HOMO band is half filled, thereby the lower branch is fully filled and the upper branch is empty. The Fermi level is located at $k_c = \pi/c$. Since the band is folded, there are two kinds of optical transitions: the intra-band transition (A) which is polarized along the c-axis and the inter-band transition (B) which is proved to be polarized along the b-axis.

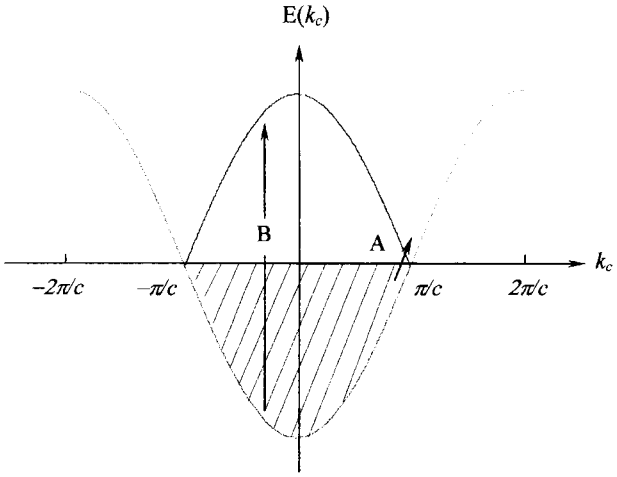

Fig. 4. One-dimensional tight-binding band of DMTSA–BF_4. The band is occupied up to $E(k_c) = 0$.

The intra-band transition is formulated into a Drude term in the extended zone $-2\pi/c \leq k_c \leq 2\pi/c$.[20] The z-component of conductivity tensor is given by the following equation,

$$Re\{\sigma_{zz}^{\mathrm{Drude}}(\omega)\} = \frac{\varepsilon_0\omega_p^2\gamma}{\omega^2+\gamma^2} \tag{7}$$

where ω_p is the plasma frequency, γ the relaxation rate. The conductivity tensor for the inter-band transition (B) is given by the following equation in the framework of the tight-binding approximation,[21–23]

$$\sigma_{jj}^{\mathrm{inter}}(\omega) = \frac{2i}{V\hbar^3}\sum_{i,f}\langle i|[H,P_j]|f\rangle\langle f|[H,P_j]|i\rangle \times \frac{\omega}{\omega_{f,i}(\omega^2-\omega_{f,i}^2+i\Gamma\omega)} \tag{8}$$

where j denotes x, y, or z, V is the volume of the crystal, i and f denote the initial and final states, respectively, $\omega_{f,i}$ and Γ are the resonant frequency and damping constant, respectively. P_j is the electric dipole moment along the j-direction. The formula for the dipole moment $\boldsymbol{P}$ by the point-charge approximation is $\boldsymbol{P} = \sum_l e\boldsymbol{R}_{lm}a_{lm}^{+}a_{lm}$, where $\boldsymbol{R}_{lm}$ is the

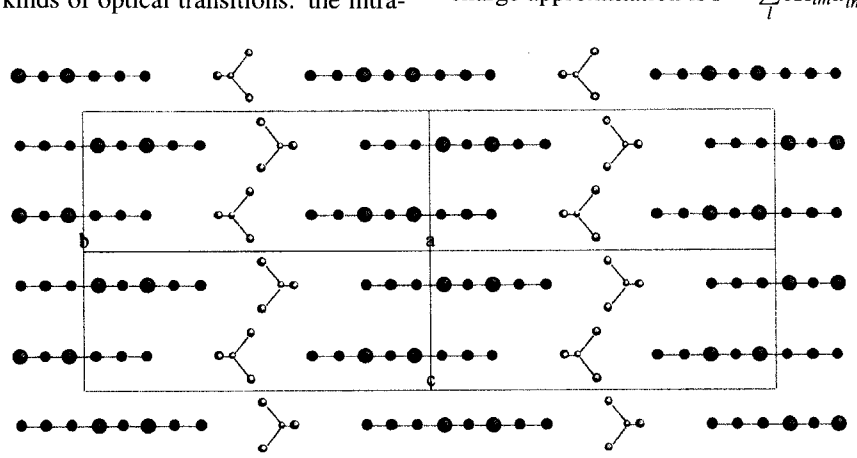

Fig. 3. Side view of the molecular stack in DMTSA–BF_4. Molecules are stacked along the c-axis in a zigzag fashion.

position vector of the m-th molecular site in the l-th unit cell. Since DMTSA has no center of symmetry, $\boldsymbol{R}_{lm}$ is defined by the center of HOMO. The tight-binding Hamiltonian H is given by the following equation,

$$H = -t_c \sum_{l,l'} \sum_{m,m'}^{2,2} a^{+}_{lm} a_{l'm'} \tag{9}$$

where l and l' denote the number of the unit cell, m and m' site numbers in the unit cell. Equation 8 is deduced to be the following equation for the j-th component of the conductivity tensor:

$$\sigma^{\text{inter}}_{jj}(\omega) = \frac{ie^2 t_c^4 \{(R^j_{l1} - R^j_{l2}) + (R^j_{l+1,1} - R^j_{l2})\}^2}{V\hbar^2} \times \sum_{k=-\pi/c}^{\pi/c} \frac{(1+\cos(k_c c))^2}{\Delta(k_c)^3} \frac{\omega}{\omega^2 - \omega_{fi}^2 + i\Gamma\omega} \tag{10}$$

$\sigma_{xx}(\omega) = 0$, because the molecules in site 1 and 2 are located on the same mirror plane perpendicular to the a-axis: $R^x_{11} = R^x_{12}$. $\sigma_{zz}(\omega) = 0$, since the molecules in site 1 and 2 are connected by the screw-axis symmetry along the c-axis, thereby having the same inter-molecular distance: $R^z_{l1} - R^z_{l2} = -R^z_{l+1,1} + R^z_{l2}$. However, $\sigma_{yy}(\omega)$ has a finite value, since the molecules are stacked in a zigzag form with a displacement δ : $\delta = |R^y_{l1} - R^y_{l2}|$. In this experiment, the polarization direction $E \perp c$ is parallel to $[1\bar{1}0]$, which makes an angle θ against the b-axis. To calculate the conductivity in this polarization direction, δ should be replaced by $\delta\cos\theta$, thereby the real part of the conductivity is given by

$$Re\{\sigma^{\text{inter}}_{\perp}(\omega)\} = \frac{e^2}{v_c} \frac{\sqrt{2} t_c (c/2)\delta^2 \cos^2\theta}{\hbar^2 \pi} \int_{-\pi/c}^{\pi/c} \frac{\sqrt{1+\cos(k_c c)}\,\omega^2 \Gamma}{\{\omega^2 - (2\Delta(k_c)/\hbar)^2\}^2 + \Gamma^2\omega^2} dk_c, \tag{11}$$

where v_c is the unit cell volume.

As we have seen in the preceding paragraph, the theoretical calculation predicts two optical transitions in this system: A is polarized parallel to the stacking axis and B is polarized along the long molecular axis. The top panel of Fig. 5 shows the observed optical conductivity spectrum, where the corresponding transitions A and B are observed. The deviation from the Drude curve comes from the structural fluctuation that will be discussed in section 4-2-2. To simulate the spectrum using Eqs. 7 and 11, we have to know ω_p, t_c, and δ. The plasma frequency of the intra-band transition A is obtained as $\hbar\omega_p(//c) = 1.15$ eV by fitting the Drude model to the high-frequency region of the observed $E//c$ reflectivity. The transfer integral t_c is obtained to be 0.2 eV using the following relation for the one-dimensional tight-binding band,[24]

$$\omega_p^2(//c) = \frac{e^2 Z}{\varepsilon_0 v_c} \frac{c^2 t_c \sin(\pi\rho/2)}{\hbar^2 \pi\rho}, \tag{12}$$

where Z (= 4) is the number of molecules in a unit cell, ρ (= 1) the charge (valence) of the molecule. The plasma frequency of the inter-band transition B is calculated by the integrated intensity,

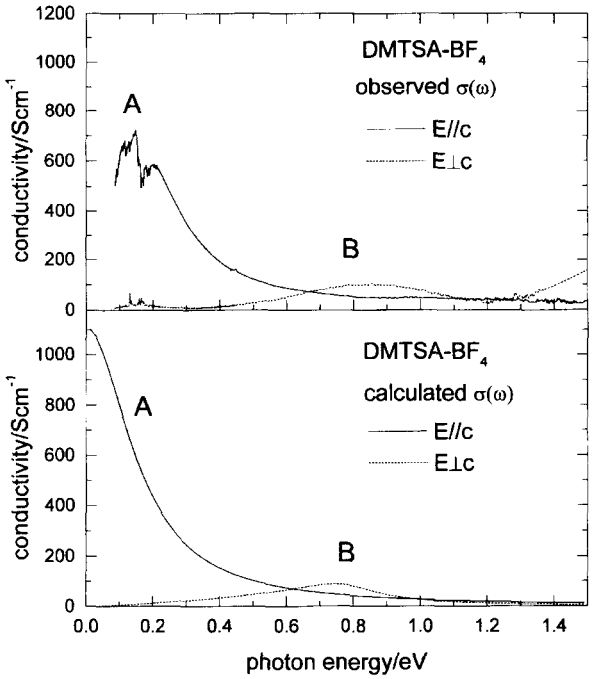

Fig. 5. Observed and calculated optical conductivity of DMTSA–BF_4. The calculation is based on the one-electron theory.

$$\omega_p^2(\perp c) = \frac{2}{\varepsilon_0 \pi} \int_0^{\infty} Re\{\sigma^{\text{inter}}_{\perp}(\omega)\} d\omega. \tag{13}$$

Using the cut-off frequency of 1.2 eV, the plasma frequency is obtained as $\hbar\omega_p(\perp c) = 0.51$ eV. On the other hand, the following relation is theoretically derived if we insert $\sigma^{\text{inter}}_{\perp}(\omega)$ given by Eq. 11 into Eq. 13,

$$\frac{\omega_p^2(\perp c)}{\omega_p^2(//c)} = \frac{(\delta\cos\theta)^2}{(c/2)^2} \tag{14}$$

Applying the experimentally obtained plasma frequencies and $c/2 = 3.385$ Å, one can calculate $\delta\cos\theta$ to be 1.49 Å. This relation means that the inter-band transition B is observable only when the stacking pattern is zigzag and the intensity of this optical transition is proportional to $t_c\delta^2$. The bottom panel of Fig. 3 shows the conductivity spectra numerically calculated by Eqs. 7 and 11. The agreement between them is excellent.

Let us examine the validity of δ obtained by Eq. 14. Since θ is the angle between $[1\bar{1}0]$ and b-axis, δ is calculated to be 1.97 Å. From this δ value, we calculate the center of the distribution of HOMO of DMTSA and compare it with the molecular orbital calculation. We calculate the distribution of HOMO of $DMTSA^0$ using the Extended Huckel method in the HyperChem-R5.1 program system. The calculated center of HOMO is close to the observed one and shifts only by 0.5 Å. The same zigzag stacking pattern exists in Bechgaard salts as well. However, the interpretation of an optical transition like the band B has not been presented yet. Jacobsen et al. reports the $E//b'$ reflection spectrum of

$(TMTSF)_2AsF_6$, and finds a clearer hump at 10000 cm^{-1}.[25] This position coincides with the bandwidth of this compound. This hump seems to be the same optical transition as the band B, although it is assigned to a forbidden transition within the TMTSF cation radical. To the best of our knowledge, this is the first observation which proves the existence of the optical transition between the branches of HOMO band.

2-2. Quasi-One-Dimensional System: DMTSA–BF_4 in Insulating Phase.[26] In this section, we will discuss the optical conductivity in the insulating phase of DMTSA–BF_4. Figure 6 shows the transitions A (top) and B (bottom) at room temperature and 10 K. The room-temperature curve of the transition A is different from that of the Drude model. As already described before, this is caused by the fluctuation of the dimerization due to the Peierls instability. At 10 K, this absorption band is remarkably enhanced with a rich phonon structure.[27] Since the gap is open below 150 K (see the inset of Fig. 7), the Drude term vanishes and the spectral weight shifts to the mid-infrared region, as shown in the top panel of Fig. 6. The enhancement of this mid-infrared band comes from the increase of the transfer integral as a result of the lattice contraction. According to the tight-binding approximation, the upper $E_+(k_c)$ and lower $E_-(k_c)$ bands are given by the following equation,

$$E_\pm(k_c) = \pm\Delta(k_c) = \pm\sqrt{t_1^2 + t_2^2 + 2t_1t_2\cos(k_cc)}, \qquad (15)$$

where t_1 and t_2 are the transfer integrals in the dimerized stack. In this model, the band gap is given by $2|t_1 - t_2|$. The low-temperature mid-infrared band is regarded as the optical transition from the lower to upper bands near $k_c = \pm\pi/c$,

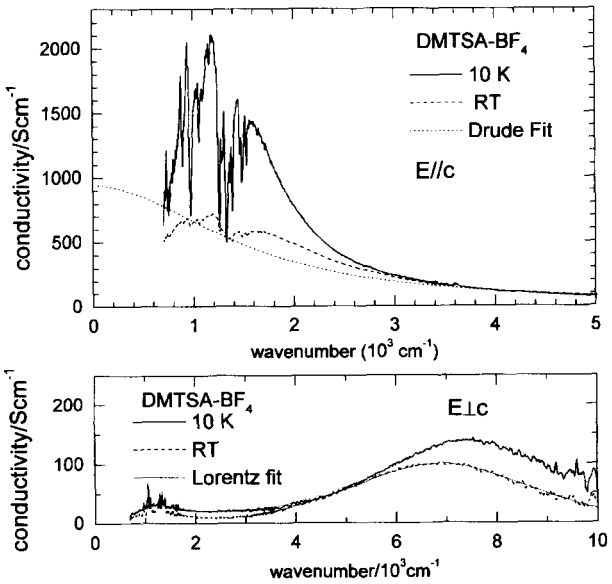

Fig. 6. Comparison of the optical conductivity of DMTSA–BF_4 in the metallic and insulating phases.

at which the transition probability is highest. The observed spectrum shows an asymmetric line shape with a tail in the high-energy side, although the strong phonon structure disturbs this electronic transition. The optical transition B shifts to the high-energy side, accompanying the enhancement of the intensity, as shown in the bottom panel of Fig. 6 as well. The excitation energy of this band determined from the Lorentz fit of $\sigma(\omega)$ is 0.85 eV at room temperature and 0.93 eV at 10 K. This absorption band polarized along the

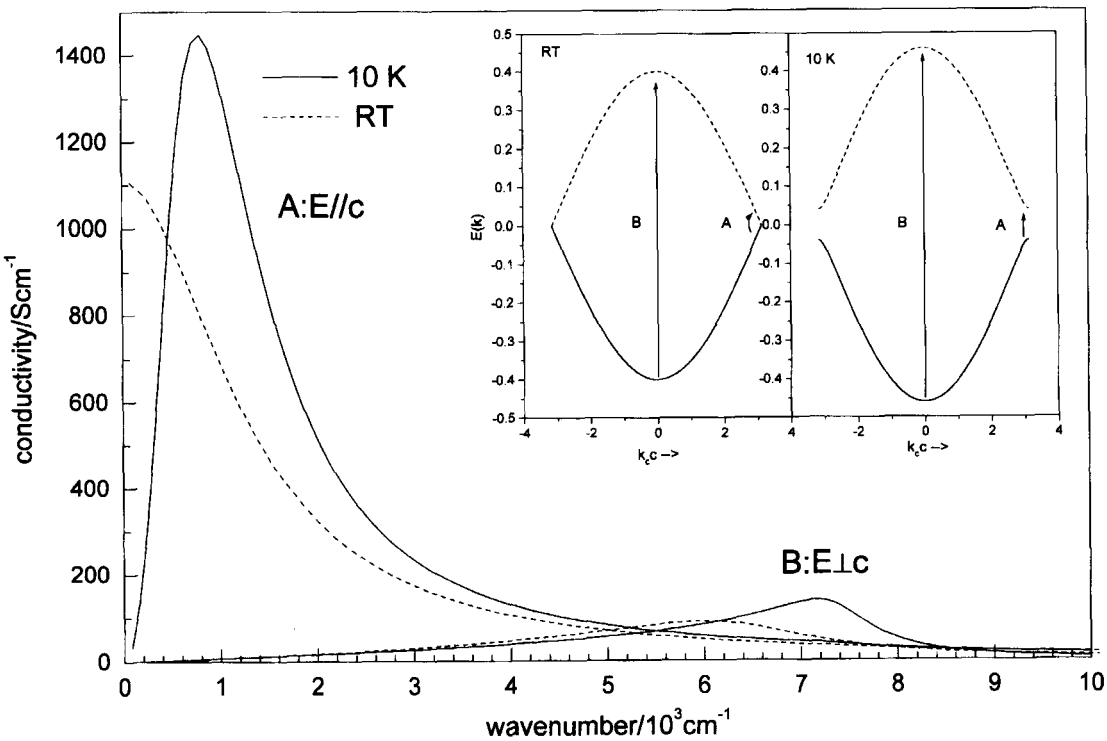

Fig. 7. Calculated optical conductivity of DMTSA–BF_4 in the metallic and insulating phases (See Fig. 6). The inset shows the band structures of the metallic (left) and insulating (right) phases.

b-axis is regarded as the optical transition B at $k_c = 0$ (see the inset of Fig. 7).

Let us simulate these characteristic changes through the metal-insulator transition in the framework of tight-binding approximation. To obtain the transfer integrals, t_1 and t_2, we estimate the plasma frequency (integrated intensity) of the transition A as $\hbar\omega = 1.22$ eV with the aid of Eq. 13 integrating from 0.65×10^3 cm^{-1} to 8×10^3 cm^{-1}. By use of Eq. 10, the optical conductivity $\sigma_{zz}(\omega)$ along the stacking direction is derived in the following way,

$$Re\{\sigma_{zz}^{\text{inter}}(\omega)\} = \frac{e^2}{v_c}\frac{(c/2)}{\hbar^2\pi}\int_{-\pi/c}^{\pi/c}\frac{\{-c_1t_1^2+c_2t_2^2-(c_1-c_2)t_1t_2\cos(k_cc)\}^2\omega^2\Gamma}{\Delta(k)^3[\{\omega^2-(2\Delta(k_c)/\hbar)^2\}^2+\Gamma^2\omega^2]}dk_c. \quad (16)$$

When one inserts Eq. 16 into Eq. 13, the plasma frequency of the optical transition A is theoretically expressed by the following equation,[28]

$$\omega_p^2 = \frac{e^2}{\varepsilon_0 v_c\hbar^2\pi}\times\left\{(c_1^2-c_2^2)(t_1-t_2)K\left(\frac{2\sqrt{t_1t_2}}{t_1+t_2}\right)+(c_1^2+c_2^2)(t_1+t_2)E\left(\frac{2\sqrt{t_1t_2}}{t_1+t_2}\right)\right\} \quad (17)$$

where, c_1 and c_2 are the inter-molecular spacing along the dimerized chain, v_c the volume of the molecular unit DMTSA–BF_4, $K(x)$ the complete elliptic integral of the first kind, $E(x)$ the complete elliptic integral of the second kind. Assuming that the band gap is equal to twice the activation energy of the resistivity and $c_1 = c_2 = c/2$, t_1 and t_2 are estimated to be 0.25 and 0.21 eV. Figure 7 shows $\sigma_{zz}(\omega)$ and $\sigma_{yy}(\omega)$ at room (broken line) and low (solid line) temperatures. This calculation reproduces the asymmetric line shape of the transition A, and the high-energy shift and intensity enhancement of transitions A and B.

2-3. Quasi-Two-Dimensional System: (BDT–TTP)$_2$X (X = AsF$_6$, SbF$_6$). The charge-transfer salts of BDT–TTP (2,5-bis(1,3-dithiol-2-ylidene)-1,3,4,6-tetrathiapentalene) provide many stable metals down to liquid helium temperature.[29,30] The stable metallic property was regarded as the result of the small on-site Coulomb energy and the strong inter-chain interaction.[29,30] The isostructural (BDT–TTP)$_2$X (X = SbF_6, AsF_6) belongs to these stable metallic groups. As shown in the top panel of Fig. 8, the arrangement of molecules is the so-called β-type which resembles Bechgaard salts (TMTSF)$_2$X (TMTSF = tetramethyltetraselenafulvalene).[31] The molecule is stacked in a slightly dimerized fashion. Since a strong hopping interaction is anticipated along the side-by-side direction as well as the stacking direction, BDT–TTP forms a conducting sheet in the (010) plane. Each conducting sheet is separated from the other by counter anions. One hole is provided by the counter anion per a unit cell, thereby a quarter-filled band is formed. The hole is confined in this conducting sheet and forms a quasi-two-dimensional band. The energy band is split into two branches, as the unit cell contains two molecules. The

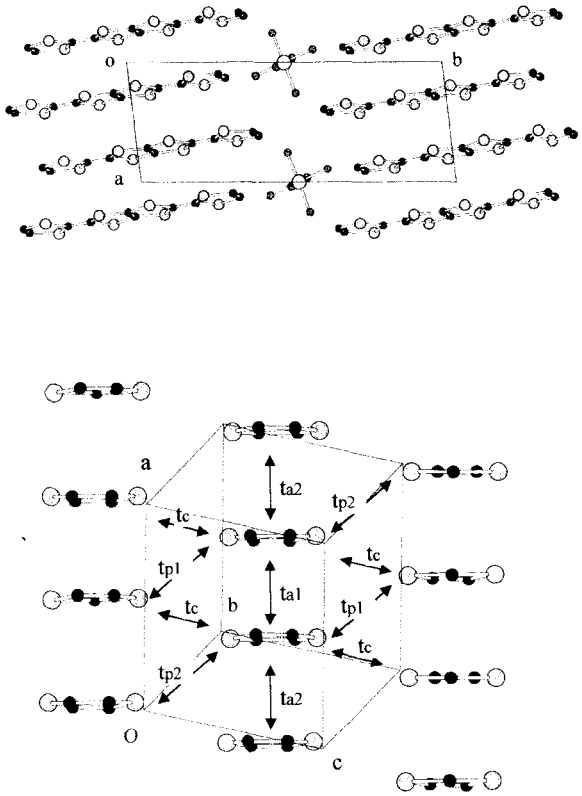

Fig. 8. Crystal structure (top) of (BDT–TTP)$_2$SbF$_6$. The bottom figure shows the molecular arrangement viewed from the long molecular axis and transfer integrals.

bottom of Fig. 8 shows the transfer integrals composing the two-dimensional network. According to the tight-binding approximation, the eigen value of the two-dimensional energy band is given by the following equation,

$$E(k_a,k_c) = 2t_c\cos(k_cc) \pm |H_{12}|, \quad (18)$$

where

$$H_{12}^2 = t_{a1}^2+t_{a2}^2+t_{p1}^2+t_{p2}^2+2t_{a1}t_{a2}\cos(k_aa)+2(t_{a1}t_{p1}+t_{a2}t_{p2})\cos(k_cc) + 2(t_{a1}t_{p2}+t_{a2}t_{p1})\cos(k_aa+k_cc)+2t_{p1}t_{p2}\cos(k_aa+2k_cc),$$

and a and c are the lattice constants, k_i ($i = a$ or c) is the reciprocal vector running over the first Brillouin zone. The transfer integrals of (BDT–TTP)$_2$SbF$_6$ are estimated to be $t_{a1} = -0.251$, $t_{a2} = -0.253$, $t_c = -0.008$, $t_{p1} = -0.079$, and $t_{p2} = -0.086$ eV.[29] Such numerical values provide the band structure, density of state (DOS), and the closed Fermi surface shown in Fig. 9.

To examine the above calculation, the reflection spectroscopy is a powerful tool. Figure 10 shows the polarized reflection spectra measured on the (010) crystal face of (BDT–TTP)$_2$SbF$_6$. Drude-like dispersions appear in both polarization directions with a remarkable anisotropy. Both of them can be satisfactorily fitted by a Drude model except the hump at 1380 cm^{-1} in the $E//a$ spectrum and the dispersion by local phonon absorption in the $E\perp a$ spectrum. The best-fit curves by the Drude model are drawn by broken lines in the same figures. This observation ensures that the one-electron

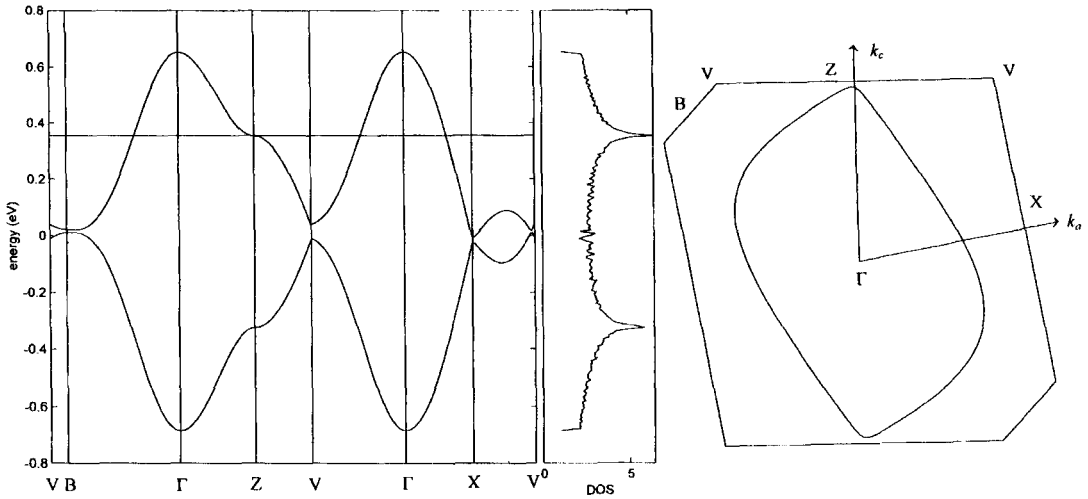

Fig. 9. Energy dispersion, density of state, and Fermi surface calculated based on the transfer integrals given by Misaki et al.[29]

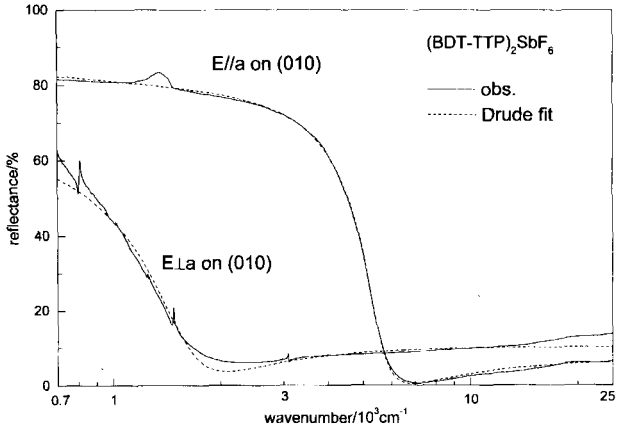

Fig. 10. Polarized reflection spectra of (BDT–TTP)$_2$SbF$_6$. Drude model can be fitted in a wide spectral range.

band picture is applicable to this compound in this spectral range. The plasma frequencies are obtained from this fitting curve as $\hbar\omega_p(//a) = 1.15$ eV for $E//a$ and $\hbar\omega_p(\perp a) = 0.39$ eV for $E\perp a$. For the more quantitative comparison, the plasma frequency is calculated using the transfer integrals shown above. The plasma frequency in a two-dimensional metal is given by the following equation,[32]

$$\omega_p^2(i) = \frac{ne^2}{\varepsilon_0\hbar^2}\frac{\int\int f(E(k_ak_c))\dfrac{\partial^2 E(k_ak_c)}{\partial k_i^2}\mathrm{d}k_a\mathrm{d}k_c}{\int\int f(E(k_ak_c))\mathrm{d}k_a\mathrm{d}k_c}, \qquad (19)$$

where n is the hole density, $f(E)$ the Fermi–Dirac function, and k_i ($i = //a, \perp a$) the wave vector along the polarization direction. We divided the first Brillouin zone into 200×200 meshes, and numerically integrated the second derivatives of $E(k_a,k_c)$ along the polarization direction assuming $T = 0$ K for the distribution function. The calculated results are $\hbar\omega_p(//a) = 1.16$ eV and $\hbar\omega_p(\perp a) = 0.75$ eV. The agreement for $E//a$ is surprisingly good, but that for $E\perp a$ is not sufficient: $\hbar\omega_p(\perp a)$ is almost twice as large as the experimental value, that is, the actual material is more anisotropic. The disagreement of the plasma frequency is attributed to the overestimation of the inter-chain transfer integrals t_{p1}, t_{p2}, and t_c in Fig. 8. The theoretical calculation predicts that t_{a1} is nearly equal to t_{a2}, t_{p1} is also close to t_{p2}, and t_c is an order of magnitude smaller than t_{p1} and t_{p2}. So the following is a good approximation: $t_{a1} = t_{a2} = t_a$, $t_{p1} = t_{p2} = t_p$, and $t_c = 0$. Under this approximation, $E(k_a, k_c)$ is expressed by only two parameters, t_a and t_p. Then t_a and t_p are obtained by numerically solving the simultaneous Eq. 19 for $\omega_p(//a)$ and $\omega_p(\perp a)$. The best solution is the set of $t_a = -0.26$ eV and $t_p = -0.048$ eV, which gives $\hbar\omega_p(//a) = 1.15$ eV and $\omega_p(\perp a) = 0.40$ eV. As we anticipated, the agreement with the calculation along the stack (t_{a1} and t_{a2}) is surprisingly good but the theoretical calculation overestimates the inter-stack transfer integrals (t_{p1}, t_{p2}, and t_c); the value is almost twice as large as that observed. We analyzed the low-temperature reflectance spectra in the same way using the room-temperature lattice constants and the two-parameter model. Figure 11 shows the temperature dependence of $|t_a|$,$|t_p|$ and their anisotropic ratio t_a/t_p. If one lower the temperature, $|t_a|$ (intra-stack direction) increases remarkably, whereas $|t_p|$ (inter-stack direction) does not change at all. The anisotropic ratio t_a/t_p increases on lowering temperature; such a result means that the (BDT–TTP)$_2$SbF$_6$ approaches a more one-dimensional system at low temperature.

Figure 12 shows the energy dispersion, density of state, and Fermi surface calculated using the transfer integrals experimentally obtained at room temperature. In contrast to the theoretical prediction, the Fermi surface is open in the k_c direction. This difference is attributable to the energy at the Z point which is determined by the difference of the intra-stack (t_a) and inter-stack (t_p) transfer integrals as $E_z = -2t_c \pm |(t_{a1}+t_{a2}) - (t_{p1}+t_{p2})|$. Since the theoretical calculation overestimates t_{p1} and t_{p2}, the energy of the upper band at the Z point is lower than the experimentally estimated E_z, and thus it becomes slightly lower than the Fermi energy, which makes the Fermi surface closed. In this compound the energy of the upper band at Z point is close to the Fermi energy, so the small difference of the transfer integrals exert a big influence on the shape of the Fermi surface near

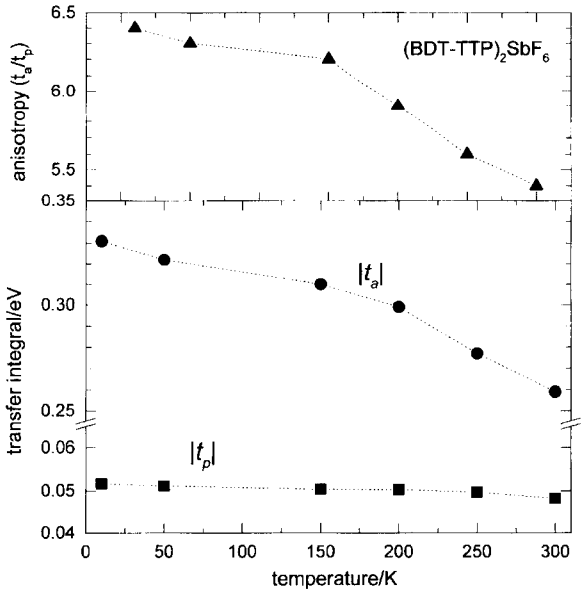

Fig. 11. Temperature dependence of the transfer integrals t_a and t_p (bottom) and their ratio (top) in $(BDT\text{–}TTP)_2SbF_6$. On lowering temperature, the anisotropy increases in this compound.

the Z point. As described in the first paragraph of section 2-3, the pattern of molecular arrangement in the conducting sheet resembles that of a Bechgaard salt, e.g. $(TMTSF)_2PF_6$.

The structural features to characterize these compounds are the anisotropy of the Fermi surface and the degree of dimerization. The dimensionality of the system is characterized by the effective mass ratio $m^*_{//}/m^*_{\perp}$ that ranges from 0 (one-dimension) to 1 (two-dimension), where the effective mass is defined as $m_i^* = ne_2/\varepsilon_0\omega_p(i)^2$. The ratios $m^*_{//}/m^*_{\perp}$ are 0.11 (300 K) and 0.08 (10 K) for $(BDT\text{–}TTP)_2SbF_6$, while it is 0.04 (100 K) for $(TMTSF)_2PF_6$[33]. The dimensionality of BDT–TTP salts is significantly higher than $(TMTSF)_2PF_6$. The dimerization is expressed by the ratio t_{a1}/t_{a2}, which is 1.0 for $(BDT\text{–}TTP)_2SbF_6$ and 1.20 for $(TMTSF)_2PF_6$. The strong dimerization gives rise effectively to a half-filled band in the 3/4-filled band, which enhances the correlation effect.[7] In this sense $(BDT\text{–}TTP)_2SbF_6$ is almost free from such a dimerization effect. $(BDT\text{–}TTP)_2SbF_6$ is characterized by the more two-dimensional band and more weakly dimerized structure than Bechgaard salt, both of which decrease the correlation effect in this system and contribute to the stable metallic state. We have performed similar analyses on other $(BDT\text{–}TTP)_2X$ ($X = AsF_6$, ClO_4, ReO_4), and selenium analogues $(ST\text{–}TTP)_2AsF_6$ and $(BDS\text{–}TTP)_2AsF_6$.[34] As shown in Table 1, the characteristic feature of the band structure is essentially the same as that for the typical compound $(BDT\text{–}TTP)_2SbF_6$. Usually the introduction of selenium atoms increase the transfer integrals both in the intra- and inter-stack directions like the relationship between TMTTF

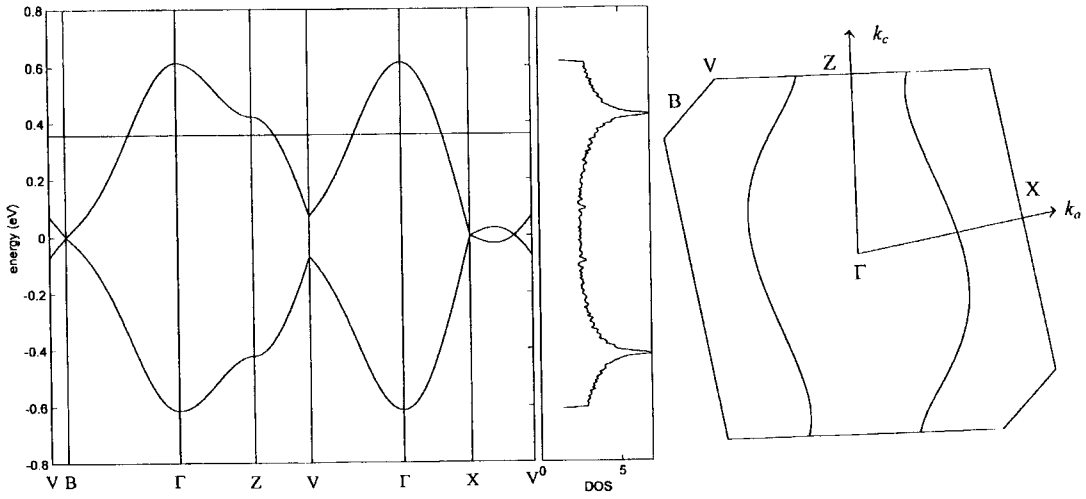

Fig. 12. Energy dispersion, density of state, and Fermi surface calculated based on the transfer integrals obtained from the analysis of the reflection spectra. See Fig. 9.

Table 1. Transfer Integrals Obtained from the Analysis of the Reflectivity Assuming $t_{a1} = t_{a2}$, $t_{p1} = t_{p2}$, $t_c = 0$ and from the Calculation of the Overlap Integrals

		t_{a1}	t_{a2}	t_{p1}	t_{p2}	t_c
$(BDT\text{–}TTP)_2SbF_6$	expt	-0.25_9	-0.25_9	-0.04_8	-0.04_8	0
	calcd	−0.251	−0.253	−0.079	−0.086	0.008
$(BDT\text{–}TTP)_2AbF_6$	expt	-0.24_4	-0.24_4	-0.04_0	-0.04_0	0
	calcd	−0.254	−0.255	−0.074	−0.086	0.005
$(ST\text{–}TTP)_2AsF_6$	expt	-0.22_1	-0.22_1	-0.04_0	-0.04_0	0
	calcd	−0.212	−0.210	−0.075	−0.058	0.010
$(BDS\text{–}TTP)_2AsF_6$	expt	-0.25_5	-0.25_5	-0.04_4	-0.04_4	0

and TMTSF.[35] However, the introduction of the outer selenium atom is not effective for the increase of the transfer integrals.

3. Optical Transition in Strongly Interacting Electron System: Hubbard Model

3-1. Half-Filled Band System: DMTTA–BF_4.[16] As shown in the inset of Fig. 13, DMTTA is a sulfur analog of DMTSA, and the charge-transfer salt DMTTA–BF_4 is isostructural to DMTSA–BF_4. In terms of one-electron theory, DMTTA–BF_4 is expected to have the same metallic band structure as DMTSA–BF_4. In contrast to the Drude-like spectrum in DMTSA–BF_4, the room-temperature optical conductivity $\sigma(\omega)$ of DMTTA–BF_4 has a peak at ca. 2000 cm^{-1} and decreases toward $\omega = 0$ as shown in Fig. 13. This spectrum means that the optical gap is open already at room temperature. The peak energy is about twice as large as that of the 10 K DMTSA–BF_4. Therefore the gap is produced by the on-site Coulomb energy (correlation gap). On lowering temperature, the spectral weight shifts to the low-energy side as shown in Fig. 13. The line shape is almost symmetric and thus different from the asymmetric shape of DMTSA–BF_4. DMTTA–BF_4 undergoes a spin Peierls transition at ca. 100 K, and forms a dimerized stack structure. Equations 3 and 4 are applicable only to the non-dimerized system. We therefore analyze the room-temperature spectrum with a uniform stack structure. The plasma frequency is experimentally obtained as 0.83 eV by the numerical integration of room-temperature $\sigma(\omega)$ from 600 cm^{-1} to 8000 cm^{-1} (see Eq. 13). As described in the introduction, the gap energy is not known from the optical spectrum, since the transition probability has not been theoretically formulated in the Hubbard model. We speculate that the gap energy is less than the peak energy (0.3 eV) of $\sigma(\omega)$ but larger than the gap energy estimated from the activation energy of the resistivity ($E_G \approx 87$ meV). Combining the gap energy with plasma frequency given by Eqs. 3 and 4, we estimate (i) $U = 0.38$ eV and $t = 0.12$ eV for $E_G \approx 87$ meV and (ii) $U = 0.74$ eV and $t = 0.15$ eV for $E_G \approx 0.3$ eV. The actual Hubbard parameters seem to be in-between. These parameters give the maximum excitation energy $E(\pi,\pi)+4t = 0.57$ eV for the case (i) and 0.9 eV for the case (ii), which corresponds to the energy difference between the bottom of the lower Hubbard band and the top of the upper Hubbard band.

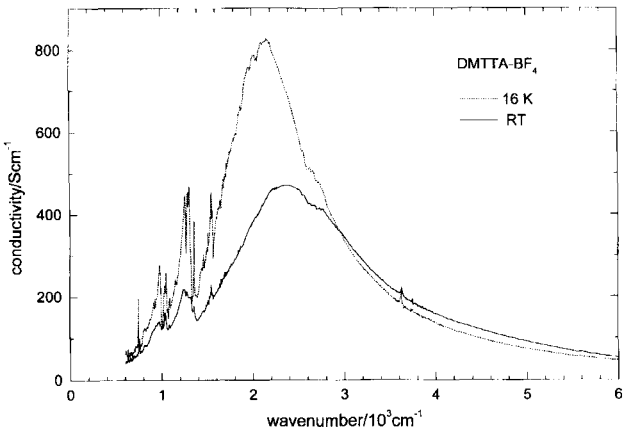

Fig. 13. Optical conductivity spectra of DMTTA–BF_4 at room temperature and 16 K.

3-2. Quarter-Filled Band System: (BEDT–ATD)$_2$-PF_6(DHF).[36,37] Let us see the optical spectrum of a quasi-one-dimensional narrow band system BEDT–ATD (4,11-bis(4,5-ethylenedithio-1,3-dithiol-2-ylidene)-4,11-dihydroanthra[2,3-c] thiadiazole). BEDT–ATD is a non-planar molecule with a butterfly-shape which shows a very small potential difference (90 mV) between the first and second oxidation potentials.[38,39] This potential difference is regarded as a measure of the on-site (on-molecule) Coulomb energy U. On the other hand, the transfer integrals are likely to be very small, since the non-planar shape prevents the large overlap of HOMO. Because of the small U, the charge-transfer salt (BEDT–ATD)$_2$$PF_6$(DHF) manages to be metallic. The intra-band transition of this compound shows a very different shape from Drude model.

The crystal of (BEDT–ATD)$_2$$PF_6$(DHF) belongs to a monoclinic system with a space group of $P2_1/a$,[38] where DHF (2,5-dihydrofuran) is the solvent molecule occluded in the crystal. As shown in Fig. 14, the unit cell consists of two molecular columns elongated along the b-axis. The repeating unit in each column is the two BEDT-ATD molecules, which are connected by the screw axis running along the b-axis. The conducting axis is parallel to the b-axis in this compound. These columns are connected by the S–S contact shown in Fig. 14. So BEDT–ATD appears to form a conducting sheet parallel to the (100) plane. Based on this crystal structure, the two-dimensional tight-binding band is presented by Imaeda et al.[40] They present the transfer integrals $t_b = -0.056$, $t_p = 0.016$, and $t_c = -0.0015$ eV, where t_b is the transfer integral along the b-axis, t_p and t_c inter-stack direction.[40] The tight-binding band $E(k_b,k_c)$ is given by the following equation.

$$E(k_b,k_c) = 2t_c\cos(k_c c) \pm 2\cos(k_b b/2)\sqrt{t_b^2 + t_p^2 + 2t_b t_p \cos(k_c c)}. \quad (20)$$

Figure 15 shows the optical conductivity spectra polarized parallel and perpendicular to the conducting b-axis. The intra-band absorption is found only in the $E//b$ spectrum which does not have a Drude-like shape, although this compound is a metal. This spectrum indicates that this compound can be regarded as a quasi-one-dimensional conductor along the b-axis. Therefore t_p and t_c must be negligibly small compared with t_b. From the comparison with the solution spectrum of this compound, the 4.2×10^3 cm^{-1} band in the $E\perp b$ spectrum is assigned to the intra-molecular excitation of BEDT–ATD^+ cation radical. It is surprising that the intra-molecular excitation has such a low-excitation energy. This is associated with the extended π-conjugation over the whole non-planar molecule. The plasma frequency provides information about the bandwidth of the conduction band. To estimate the plasma frequency, we use Eq. 13 by extrapolating $\sigma(\omega)$ to $\sigma(0) = 30$ S cm^{-1} (dc conductivity at room

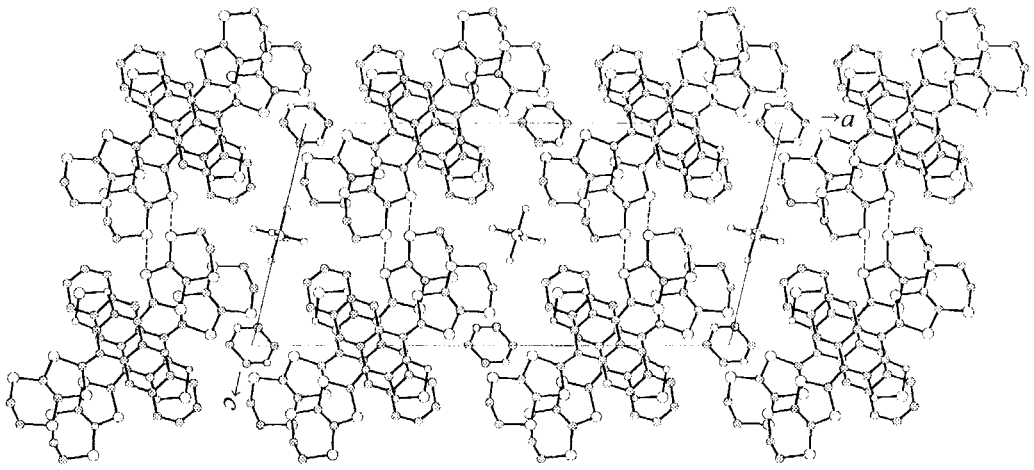

Fig. 14. Crystal structure of $(BEDT\text{–}ATD)_2PF_6(DHF)$. DHF molecules at the center of symmetry are disordered.

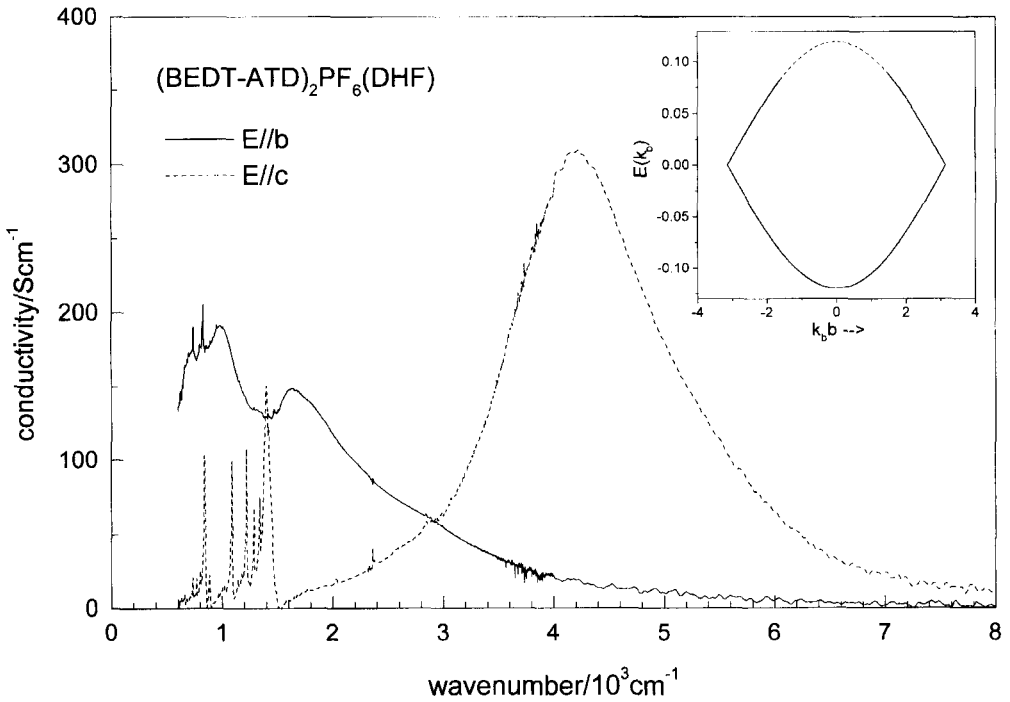

Fig. 15. Optical conductivity spectra of $(BEDT\text{–}ATD)_2\ PF_6(DHF)$. The inset shows the one-dimensional 3/4-filled band in tight-binding approximation. The 4000 cm^{-1} band in the *E//c* spectrum is the local (intra-molecular) excitation.

temperature) by a straight line and the cut-off frequency is taken as $5\times10^3\,cm^{-1}$. The plasma frequency estimated in this method is $\hbar\omega = 0.45$ eV. Using the relation (See Eq. 12) between plasma frequency and transfer integral in one-dimensional case, we estimate t_b to be 0.06 eV. The bandwidth $4t_b = 0.24$ eV is extremely narrow among the organic metals. It is surprising that such a narrow-band and quasi-one-dimensional system becomes a metal.

The narrow band given by the optical spectrum suggests some correlation effect to the optical conductivity. In fact room-temperature $\sigma(\omega)$ is very different from the Drude-like curve as already described before. Contrary to the Drude model, the low-wavenumber side of room-temperature $\sigma(\omega)$ is not rising up but falling down to the dc conductivity value ca. 30 $S\,cm^{-1}$, making broad peaks around 1000 cm^{-1} and 1700 cm^{-1}. Similar spectral features are observed in metallic β-$(BEDT\text{–}TTF)_2I_3$[41] as well. In this case, two molecules in the unit cell are dimerized and thus the conduction band is split into two branches. The optical transition from the lower to upper branches is overlapped in the Drude term. Due to this inter-branch transition, the Drude term is hidden from $\sigma(\omega)$ of the infrared region. This is the reason why the line shape of $\sigma(\omega)$ in β-$(BEDT\text{–}TTF)_2I_3$ is significantly deviated from the Drude-like shape. In this compound, however, BEDT–ATD is not dimerized but uniformly stacked owing to the screw-axis symmetry, so the conduction band is folded at the zone boundary as shown in the inset of Fig. 15. In such a case, the inter-band optical transition is forbidden in the *//b* spectrum as already explained in section 2-1. Thus the double peak at 1000 cm^{-1} and 1700 cm^{-1} cannot be ex-

plained by the inter-band transition. If we take the correlation into account, the uniformly distributed charge tends to localize. The decreasing nature of $\sigma(\omega \rightarrow 0)$ is related to this charge localization.[42,43] If the equivalent fractional charge +0.5 is separated into 0 and +1, for example, the equivalent molecule becomes non-equivalent by breaking the screw-axis symmetry.[44] The double peak structure of this absorption band may be related to the fluctuation of the charge separation.[45] Recently Tajima has calculated the optical conductivity of a one-dimensional quarter-filled conductor in the framework of mean-field approximation.[46] According to his theoretical calculation, the optical transition shows a single peak when U is taken into account and $V/t < 1.5$ but double peaks when V/t is larger than 2. This calculation may explain the double peak, since the bandwidth is very narrow in this compound.

4. Detection of the Structural Change Through the Observation of the Vibronic Bands

4-1. Application of the Dimer Model to DMTSA–ClO_4.[16] The theoretical model for the vibronic coupling is described in the introduction of this article. Let us apply the dimer model to DMTSA–ClO_4 before going to the symmetry breaking during the phase transition. DMTSA–ClO_4 is a 1 : 1 charge-transfer salt with a strongly dimerized structure.[18] The dimer approximation is ensured by the ratio of inter-dimer to intra-dimer overlap integral, 0.25. The optical conductivity spectrum and the simulation by the dimer model are shown in Fig. 16. The broad band at ca. 2900 cm^{-1} in the bottom panel is the charge-transfer excitation within the dimer, and the strong phonon bands below this electronic absorption are the vibronic bands. The observed vibronic bands as well as the charge-transfer band are very well reproduced by

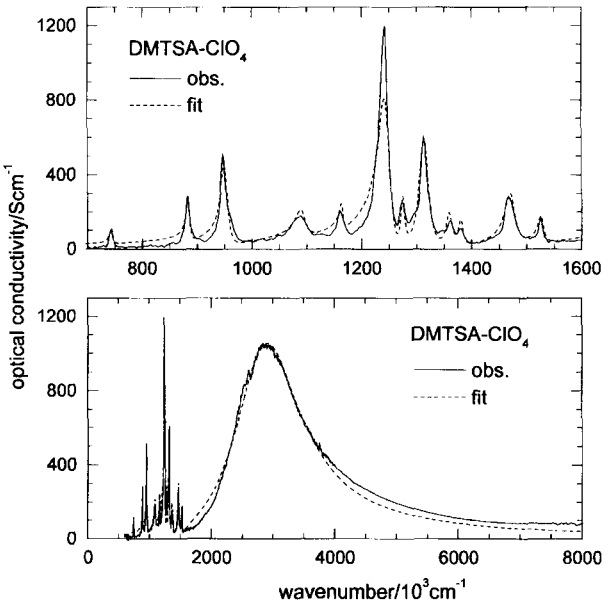

Fig. 16. Charge-transfer (broad) and vibronic (sharp) bands in DMTSA–ClO_4. The optical conductivity is well reproduced by the dimer model involving the electron-molecular vibration coupling.

Eq. 5 in the dimer model, except for the strongest band at 1242 cm^{-1}. The unperturbed frequency ω_α deduced from this analysis agrees well with the uncoupled modes which are directly observed in the Raman and infrared spectrum (See Ref. 16).[47] The sum of the coupling constant $\lambda = 0.14$ in this spectral region is much smaller than the value 0.34 of TCNQ[48] and 0.6 of TTF[49]. The magnitude of the total coupling constant is connected with the geometrical change from the neutral to ionic state of the molecule. In contrast to TCNQ and TTF, the molecular geometry of DMTSA does not change so much when it is ionized. Takimiya et al. claim that the Se–Se distance is shortened in $DMTSA^+$.[50] The coupling constant of Se–Se stretching mode is not included in λ, since it appears at a frequency lower than 600 cm^{-1}. The molecular vibrational mode having a large coupling constant often shows a large frequency shift when the molecule is ionized (oxidization or reduction). The comparison of these Raman lines between neutral DMTSA and DMTSA–ClO_4 shows a small shift within 10 cm^{-1} between the neutral and ionic state except for the 1170 cm^{-1} (11 cm^{-1}) and 1387 cm^{-1} (18 cm^{-1}) lines in DMTSA–ClO_4, which are much smaller than the shift of the charge-sensitive mode in TCNQ[51] or BEDT–TTF.[52] As described before, the Se–Se stretching mode is expected to be sensitive to the degree of oxidation from the crystal structure analysis. However, we cannot find such a charge-sensitive Raman active mode in the spectral region of 150–4000 cm^{-1}.

4-2. Emv Coupling in Quasi-One-Dimensional System. 4-2-1. Evolution of the Vibronic Bands in (BEDT–ATD)$_2$PF$_6$(DHF).[36,37] When the molecules are uniformly stacked in the crystal, the vibronic modes are fully suppressed. For the selection rule of a vibronic mode, we have to consider the induced dipole in a unit cell instead of in an isolated dimer. The theoretical study has been conducted by Bozio et al. for a half-filled one-dimensional system.[11] Let us introduce an example, (BEDT–ATD)$_2$PF$_6$(DHF), that demonstrates the breaking of the selection rule via the metal-insulator phase transition. (BEDT–ATD)$_2$PF$_6$(DHF) undergoes a metal-insulator phase transition (MI) at 150—200 K.[40] As shown in Fig. 17, the *E*//*b* spectrum shows a remarkable enhancement of the intensity of vibronic modes. The vibronic mode becomes quite obvious below 100 K. The unit cell contains four BEDT–ATD molecules with the space group $P2_1/a$, which includes the factor group of C_{2h}. The symmetry of BEDT–ATD is C_s. When we consider the breathing mode with a' symmetry in C_s point group, the four unit cell modes are classified into A_g, A_u, B_g, and B_u modes. As shown by open arrows in the inset of Fig. 17, the latter two modes induce a charge flow and thereby a dipole between the molecules along the *b*-axis. The B_g mode is infrared inactive, since the induced dipoles are cancelled with each other within the unit cell due to the inversion symmetry. The B_u mode produces a unit cell dipole along the *b*-axis. Owing to the translational symmetry (for $q = 0$ mode), another dipole is induced in the opposite direction; thus the induced dipole in the unit cell is cancelled out, when we take account of the induced dipole (open arrow) with the molecule

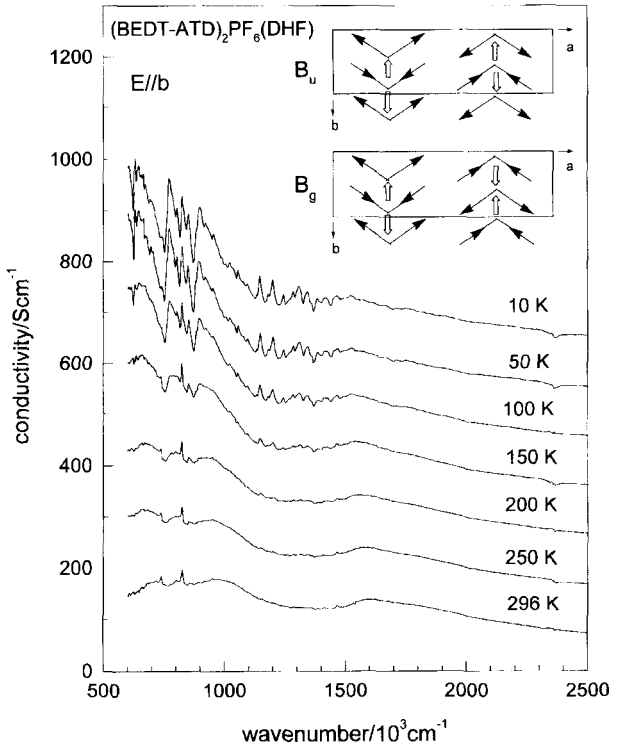

Fig. 17. Evolution of the vibronic bands during the metal-insulator phase transition at 150—200 K in (BEDT–ATD)$_2$PF$_6$(DHF). The inset shows the unit cell dipoles induced by the electron-molecular vibration coupling.

in the next unit cell. When the screw-axis symmetry is broken ($P2_1/a \rightarrow Pa$), the arrows pointing opposite directions become non-equivalent, thereby the B_u mode becomes infrared active along the b-axis. The intensity of a vibronic mode depends upon the displacement of the molecule from the position given by the symmetry. These modes are hardly observable at room temperature but begin to grow below 150 K. Therefore Fig. 17 means the breaking of the screw-axis symmetry along the b-axis below 150 K. In the analogous compound (BEDT–ATD)$_2$PF$_6$(THF), the vibronic bands are already observable above the MI transition temperature.[36] This suggests the view that the screw-axis symmetry is locally broken above the MI transition temperature in several compounds.

A low-temperature X-ray diffraction experiment was conducted on (BEDT–ATD)$_2$PF$_6$(DHF) to confirm the change of symmetry and to determine the pattern of the lattice distortion ($2k_F$ or $4k_F$) detecting the possible super-structure.[37] No spot or no diffuse streak for the doubling of the b-axis is found down to 87 K. No super-lattice along the a- and c-axes is found at 87 K as well. From the examination of the systematic absence of $h = 2n+1$ for (h0l) reflections, the glide-plane symmetry along the a-axis remains at 87 K. As for the systematic absence of (0k0) reflections at low temperature, (030) and (050) reflections are detected weakly but significantly larger than $3\sigma(F_o)$. The appearance of the (0k0) reflections with odd indices clearly indicates the breaking of screw-axis symmetry along the b-axis.

Due to the screw-axis symmetry, we can take the effective periodic unit as $b' = b/2$.[19] Accordingly, the room-temperature phase has a 3/4-filled metallic band in a non-correlated case and a half-filled metallic band in a strongly correlated case. In (BEDT–ATD)$_2$PF$_6$(DHF), the systematic absence of (0k0) $k = 2n+1$ is broken, while (h0l) $h = 2n+1$ is maintained and no super-structure is found. These results of low-temperature X-ray diffraction indicate the change of the space group from $P2_1/a$ to Pa or $P2/a$ below the MI transition temperature. Actually Pa is confirmed from the low-temperature crystal structure analysis.[37] In this space group, the screw-axis symmetry is lost, so the periodic unit is doubled from $b/2$ to b and opens a gap at $k = \pm\pi/b$. This structural change corresponds to the $4k_F$ ($= b'^*/2 = b^*$) lattice modulation (dimerization). The absence of the super-lattice with $b^*/2$ is supported by the static magnetic susceptibility which is more sensitive to this kind of lattice modulation. The $2k_F$-lattice modulation makes a tetramer in the unit cell and thus the two holes in the tetramer form a spin singlet. The $2k_F$-lattice modulation therefore brings about a non-magnetic state. In this case the paramagnetic susceptibility should vanish toward 0 K below the MI transition temperature. However, the paramagnetic susceptibility is almost temperature independent and does not show such a tendency. Therefore we conclude in this compound that the insulating phase has a lattice of $4k_F$ modulation.

4-2-2. Phase Transition in DMTSA–BF$_4$ and DMTTA–BF$_4$.[16] In this section, we will characterize the phase transitions of DMTTA–BF$_4$ and DMTSA–BF$_4$ from the viewpoint of vibronic bands. DMTSA–BF$_4$ undergoes a MI transition at ca. 150 K, which appears as an upturn in the resistivity and thermopower and a downturn in the spin susceptibility.[53] The metallic resistivity, small value of linearly decreasing thermopower, and small value of temperature-independent paramagnetic susceptibility are consistent with the one-electron picture which is pointed out from the analysis of the optical spectrum. On the other hand, DMTTA–BF$_4$ shows very different properties from DMTSA–BF$_4$. DMTTA–BF$_4$ exhibits a magnetic phase transition at ca. 100 K. However, this phase transition exerts no influence on the resistivity. The absolute value of the spin susceptibility of DMTTA–BF$_4$ is about four times as large as that of DMTSA–BF$_4$. The absolute value of thermopower is much larger than that of DMTSA–BF$_4$ as well. All these properties are consistent with the strong correlation derived from the optical spectrum.

As shown in the top panel of Fig. 18, several vibronic bands increase their intensity steeply below the phase transition temperature at 150 K. This result indicates the breaking of the screw-axis symmetry; thereby the lattice distortion such as the dimerized lattice occurs. Several vibronic modes are weakly observed even at room temperature, although the screw-axis and glide-plane symmetry is guaranteed by the space group $Cmcm$. Since the selection rule of the optical transition is determined by the local symmetry around the molecule, the symmetry breaking in a short-range area partly breaks the selection rule. So this result suggests the existence of the structural fluctuations which are expected

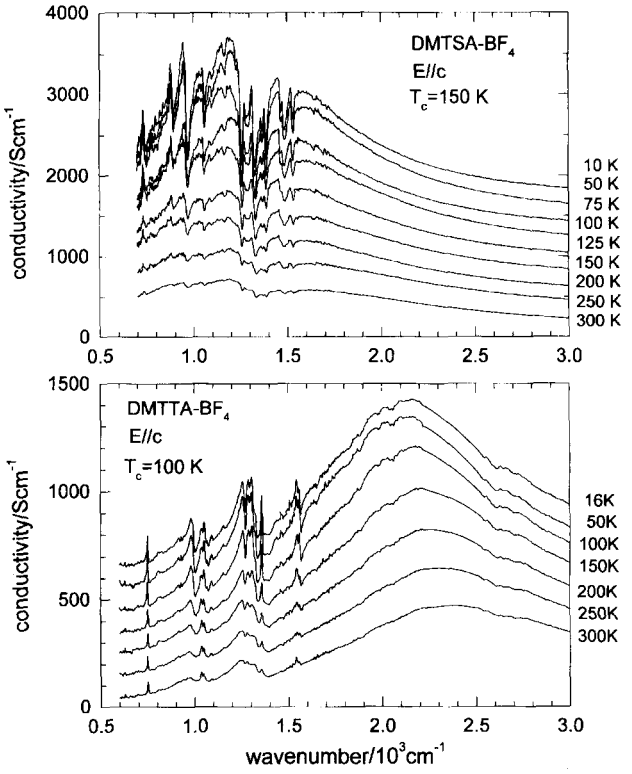

Fig. 18. Evolution of the vibronic bands during the phase transition in DMTSA–BF_4 (top) and DMTTA–BF_4 (bottom).

to be large in a quasi-one-dimensional system. Taking the magnetic and electric properties into account, the low-temperature state of DMTSA–BF_4 is considered to be the Peierls states. Recently the research group of Okayama University has carefully examined the low-temperature x-ray diffraction of DMTSF–BF_4 and DMTTF–BF_4.[54] According to their experiment, the violation of the extinction rule ($F(00\ell) = 0$ for $\ell = 2n+1$) was not detected down to 30 K in DMTSA–BF_4. The structural change may be too small to be detected by x-ray diffraction.

The bottom panel of Fig. 18 shows the temperature dependent *E//c* spectrum of DMTTA–BF_4. The vibronic modes appear as peaks in this compound, since the electronic excitation shifts to high-energy side compared with DMTSA-BF_4. Several broad peaks are found already at room temperature very clearly. According to the recent x-ray diffraction experiment,[54] the space group of DMTTA-BF_4 is not *Cmcm* but *C2/m*, where the screw-axis symmetry is very weakly broken already at room temperature. This result is consistent with the obvious appearance of the vibronic bands at room temperature. The integrated intensity of several vibronic bands is plotted against the temperature.[16] The intensity of these vibronic bands continuously increases and monotonously passes over the phase transition temperature (100 K). The precise experiment of x-ray diffraction detected no substantial peaks near the phase transition temperature at 100 K.[54] Consequently, in DMTTA–BF_4 the structural change seems to evolve continuously from room temperature. This result for the lattice instability is inconsistent with the abrupt decrease of the spin susceptibility around 100 K that suggests the spin Peierls transition. To reconcile these results, more careful and detailed experiments on the temperature dependence of x-ray diffraction, reflectivity, and spin susceptibility are necessary.

4-3. Emv Coupling in Quasi-Two-Dimensional System. The selection rule for a vibronic mode in a quasi-two-dimensional system is more complicated, since the molecules are connected by several transfer integrals in the two-dimensional unit cell. Figure 19 shows the room- and low-temperature optical conductivity of (BDT–TTP)$_2SbF_6$ and (BDT–TTP)$_2ClO_4$. The space group of (BDT–TTP)$_2SbF_6$ is $P\bar{1}$, so the factor group is C_i. The molecules 1 and 2 are connected by the center of symmetry. When we consider the intra-molecular a_g mode, the infrared active mode of the unit cell is the A_u mode as shown in the inset of the left panel of Fig. 19. This kind of anti-phase vibration induces several oscillating dipoles denoted by open arrows. The dipole along the *a*-axis is produced via the transfer integrals t_{a1} and t_{a2} (See Fig. 8). Since t_{a1} and t_{a2} are not equivalent, these dipoles do not cancell. t_{p1} and t_{p2} works oppositely like t_{a1} and t_{a2}. So the dipoles between the stacks are not cancelled as well, and contribute to the *//a* and $\perp a$ polarization. As shown in the left panel of Fig. 19, a broad dip appears at 1433 cm^{-1} (RT) and 1392 cm^{-1} (10 K) in the *E//a* spectrum. The corresponding A_u mode is detected at 1473 cm^{-1} (RT) and 1477 cm^{-1} (10 K) in the $E\perp a$ spectrum.[55] BDT–TTP has three C=C stretching a_g modes at $\nu_2 = 1555$ cm^{-1}, $\nu_3 = 1525$ cm^{-1}, and $\nu_4 = 1504$ cm^{-1}, since the molecule involves three independent C=C bonds: central ring C=C, outer ring C=C, and bridge C=C (See Fig. 1).[56] According to the theoretical estimation, the coupling constant of ν_3 is largest among these three a_g modes.[57] Consequently, the broad dip in *E//a* spectrum is assigned to the A_u mode of ν_3 molecular vibration. The conductivity curve including the dip is well reproduced by the following function:[58]

$$\sigma(\omega) = \sigma_D(\omega) + p\sigma_D(\omega)\{F(\omega) - 1\}$$
$$\sigma_D(\omega) = \frac{\varepsilon_0\omega_p^2\gamma_D}{\omega^2+\gamma_D^2}, \text{ and } F(\omega) = \frac{\{q+(\omega-\omega_0)/\gamma\}^2}{1+\{(\omega-\omega_0)/\gamma\}^2} \quad (21)$$

where $\sigma_D(\omega)$ is the real part of the conductivity of the Drude model and $F(\omega)$ is the line-shape function to describe the Fano interference effect. The parameter p represents the intensity fraction of the vibronic mode, q the inverse asymmetric parameter, ω_0 the resonance energy of the discrete state, γ the decay rate of the discrete state in the continuum state. The parameters at 10 K are $p = 0.48$, $q = 0.05$, $\omega_0 = 1390$ cm^{-1}, $\gamma = 135$ cm^{-1}. The small q indicates that this vibronic mode is strongly coupled with the conduction electron absorption. The feature of the coupling with intra-molecular vibration (local phonon) is very different from the rich vibronic bands in (TMTSF)$_2PF_6$,[25] β-(BEDT–TTF)$_2I_3$,[32] DMTSA–BF_4, and (BEDT–ATD)$_2PF_6$(DHF). It is surprising that only this mode is coupled with conduction-electron absorption band, which means that the sum of the coupling constants with local phonons will be very small in (BDT–TTP)$_2SbF_6$.

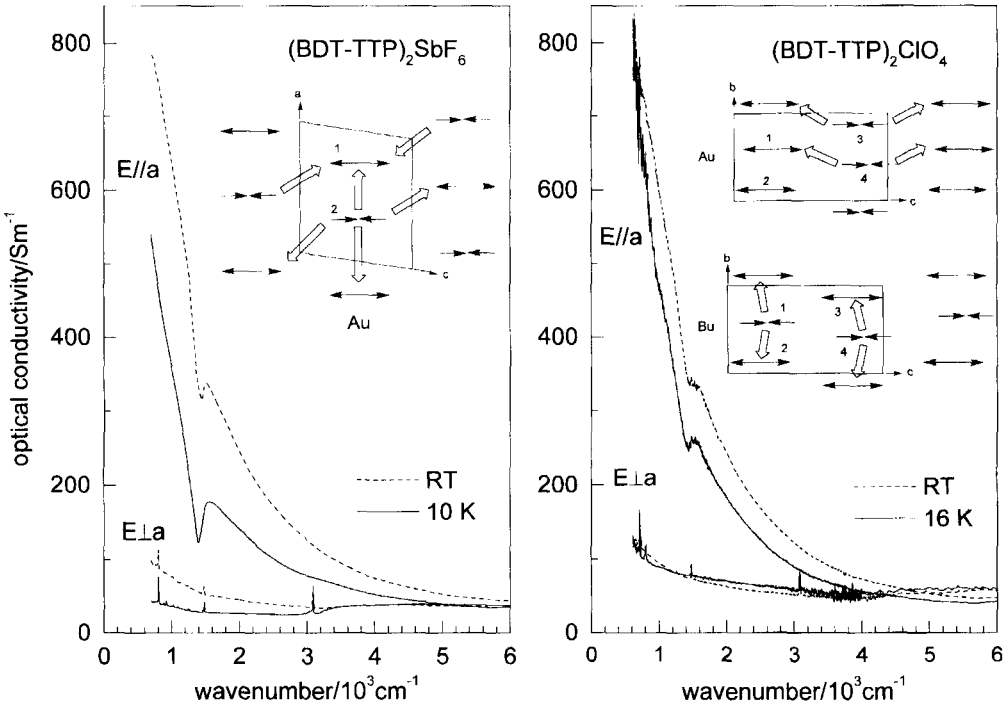

Fig. 19. Vibronic bands in quasi-two-dimensional metals $(BDT–TTP)_2SbF_6$ (left) and $(BDT–TTP)_2ClO_4$ (right). The inset shows the unit cell dipoles induced by the electron-molecular vibration coupling.

The optical conductivity of $(BDT–TTP)_2ClO_4$ is shown in the right panel of Fig. 19.[34] Compared with $(BDT–TTP)_2SbF_6$, the dips at 1462 cm^{-1} (RT) and 1437 cm^{-1} (16 K) are weak. The space group of $(BDT–TTP)_2ClO_4$ is $C2/c$, so that the factor group is C_{2h}. The molecules 1 and 3 are respectively related to the molecules 2 and 4 by the screw axis (See the inset of Fig. 19). The molecules 1 and 2 are respectively related to the molecules 3 and 4 by glide plane. When we consider the intra-molecular a_g mode, this group involves two infrared active modes A_u and B_u which are polarized along the b direction and ac plane, respectively. The transfer integrals in this crystal are the following: t_b (molecules 1 and 2) is 0.254 eV, t_{p1} (molecules 1 and 4) −0.094 eV, t_{p3} (molecules 2 and 3) −0.081 eV, and t_{p2} (molecules 1 and 3) 0.002 eV. Therefore the A_u modes produces the oscillating dipole drawn by open arrows in the inset of the right panel of Fig. 19. The B_u mode is polarized in the ac plane, since the arrows along the a-axis are equivalent and thus the a-axis component is cancelled out. As in the case of $(BDT–TTP)_2SbF_6$, the dip in the *E//a* spectrum is assigned to the A_u mode.

Finally let me give a brief comment on the interpretation of the emv coupling in metallic compound. The oscillating dipole drawn in the inset of Fig. 19 generates a fluctuation of the charge density. If the bandwidth is wide enough and the correlation effect is negligible, then such a fluctuation of the charge density will be screened out. Consequently, the observation of the dip through the emv coupling suggests that the correlation effect is working even in this compound that exhibits exceptionally (among organic metals) a Drude-like reflectivity over a wide spectral range.

5. Mixing of the Longitudinal Excitation with Transverse Excitation in a Quasi-Two-Dimensional Organic Metal: Observation of Plasmon.[59] As explained in the introduction, the plasmon of a metal cannot be directly detected by the optical method in an isotropic metal. In the anisotropic metal, however, the plasmon mixes with intraband transitions when the wavevector of the light is not parallel to the optical principal axes. So one can observe this longitudinal excitation by normal incidence reflection spectroscopy, if the crystal has several high-quality faces. In an anisotropic material, a dielectric function against a given wavevector and polarization is calculated using the dielectric function along the optical axis based on the Fresnel equation. Usually in organic conductors, however, the crystal develops mostly along the optical principal axes: it grows needle-like along the conducting axis in a quasi-one-dimensional material and develops plate-like in a quasi-two-dimensional material. So the observation of the longitudinal excitation is extremely rare. $(BO)_2Cl(H_2O)_3$ (See Fig. 1) is a quasi-two-dimensional organic metal extending its conducting sheet in the (001) plane.[60,61] The plate-like crystal has naturally a large (001) crystal face developing crystal edges [110]- and [1$\bar{1}$0]-axes. When we measure the reflectivity on the narrow side face in the direction perpendicular to the [1$\bar{1}$0]-axis, we find a new unknown peak in the near-infrared region.[62] We prove in this section that this new peak is ascribable to the plasmon absorption comparing it with the theoretical simulation.

BO molecules are arranged in the (001) plane making a conducting sheet, which is separated from the next sheet by Cl^- anions and H_2O molecules along the c-axis.[63,64] Taking into account the crystal structure, the optical properties, and the results of magneto-resistance experiment, one can regard $BO_2Cl(H_2O)_3$ as a two-dimensional metal.[65,66] Since

the crystal belongs to monoclinic system with the unique *b*-axis, and the conducting sheet is parallel to the (001) plane, the optical axes in the IR region correspond to *a*- and *b*-axes. Actually the reflectivity polarized along each axis is Drude-like and gives the maximum and minimum in the IR region. Therefore the optical axes of this compound in IR region are concluded to be *a*, *b*, and c^*, where c^* is the reciprocal axis perpendicular to the (001) plane. The $E//c^*$ spectrum is approximately given by the $E\perp[1\bar{1}0]$-on-(110) spectrum, since the angle between c^* and $\perp[1\bar{1}0]$ on (110) is only 4.1°. This spectrum has no electronic dispersion in the 600—10000 cm^{-1} region except sharp phonon dispersions. This is direct evidence for the two-dimensional band structure. We now have reflectivities along the three principal axes. The spectra obtained on the (111), and $(11\bar{1})$ planes with the polarization of $E\perp[1\bar{1}0]$ exhibit weak dispersions around 5000—6000 cm^{-1}. As shown in the top panel of Fig. 20, these dispersions are transformed into broad peaks in the optical conductivity spectra. The lowest electronic excitation of BO^+ corresponds to the dispersion at 13000 cm^{-1},[67] thereby no other intra-molecular excitation is expected around 5000 cm^{-1} region.

From the reflectivity in the (001) plane, we can draw a Fresnel ellipsoid of the dielectric function in the IR region, where the charge carriers mainly contribute to the dielectric function. The ellipsoid of the dielectric function is schematically drawn in Fig. 21. Here we denote the principal axes along *a*, *b*, and c^* as *x*, *y*, and *z*, respectively. The electronic

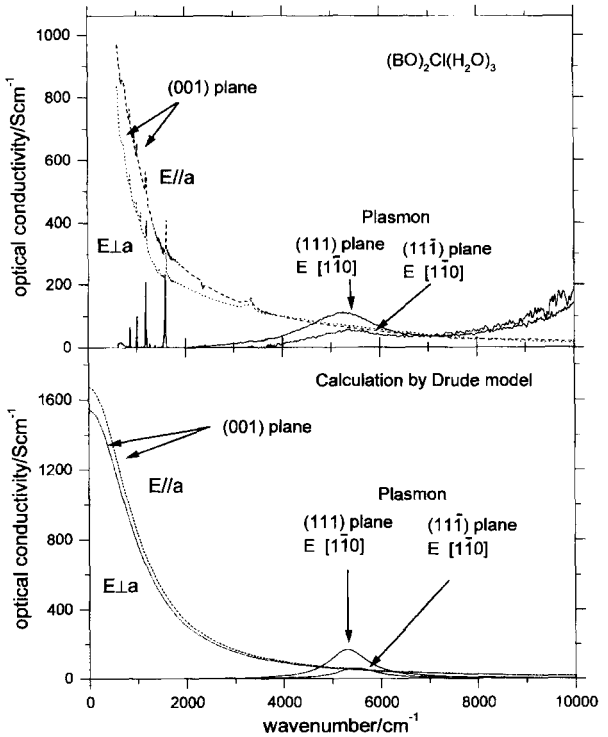

Fig. 20. Observed (top) and calculated (bottom) optical conductivity of $(BO)_2Cl(H_2O)_3$. Plasmon is detected on the side faces of the conducting plane (See text), and it is reproduced by the Drude model.

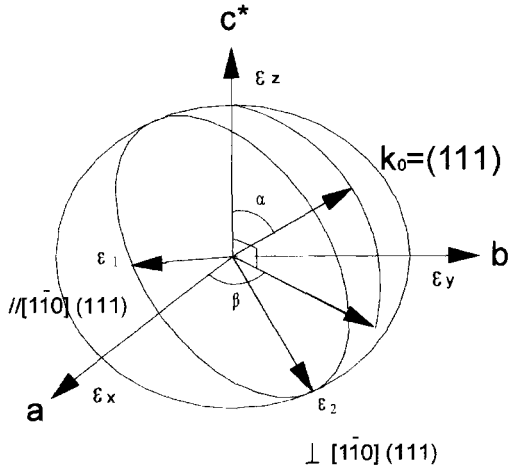

$(BO)_2Cl(H_2O)_3$

Fig. 21. Fresnel dielectric constant ellipsoid in $(BO)_2Cl(H_2O)_3$. ε_x, ε_y, ε_z are the principal values of dielectric constant tensor. ε_1 and ε_2 are the principal values on the (111) crystal face. k_0 denotes the wave vector of the incident light.

part of the dielectric function in the IR region of these principal axes are modeled by the following Drude functions in the (001) plane:

$$\varepsilon_x(\omega) = \varepsilon_x^0 - \frac{\omega_{px}^2}{\omega(\omega + i\gamma_x)} \tag{22}$$

$$\varepsilon_y(\omega) = \varepsilon_y^0 - \frac{\omega_{py}^2}{\omega(\omega + i\gamma_y)}, \tag{23}$$

where ω_{px} and ω_{py} are the plasma frequencies along the *x*- and *y*-directions, γ_x and γ_y are the scattering rate of the charge carriers along the *x*- and *y*-directions. The dielectric function along the c^* axis is approximated to be constant:

$$\varepsilon_z(\omega) = \varepsilon_z^0. \tag{24}$$

When the wave vector is parallel to the c^* axis, the dielectric functions $\varepsilon_x(\omega)$ and $\varepsilon_y(\omega)$ are responsible for the reflectivity along these two optical axes. When we measure the reflectivity using the light normal to the (111) and $(11\bar{1})$ planes, the optical axes on these planes $//[1\bar{1}0]$ and $\perp[1\bar{1}0]$ directions are given as the principal axes of the ellipse shown in Fig. 21. The principal values $\varepsilon_1(\omega)$ and $\varepsilon_2(\omega)$ along the $//[1\bar{1}0]$ and $\perp[1\bar{1}0]$ directions are obtained by solving the following Fresnel equation:

$$\frac{k_{0x}^2}{\left(\frac{1}{\varepsilon_x} - \frac{1}{\varepsilon}\right)} + \frac{k_{0y}^2}{\left(\frac{1}{\varepsilon_y} - \frac{1}{\varepsilon}\right)} + \frac{k_{0z}^2}{\left(\frac{1}{\varepsilon_z} - \frac{1}{\varepsilon}\right)} = 0, \tag{25}$$

where $\boldsymbol{k_0}$ is the unit vector along the wave vector. When we express $\boldsymbol{k_0}$ by the angles α and β defined in Fig. 21, $k_{0x} = \sin\alpha\cos\beta$, $k_{0y} = \sin\alpha\sin\beta$, and $k_{0z} = \cos\alpha$. The two solutions $\varepsilon_1(\omega)$ and $\varepsilon_2(\omega)$ are given in the following way.

$$\varepsilon_{1,2}(\alpha,\beta,\omega)^{-1} = \frac{1}{2\varepsilon_x}(1-\sin^2\alpha\cos^2\beta) + \frac{1}{2\varepsilon_y}(1-\sin^2\alpha\sin^2\beta)$$

$$+\frac{1}{2\varepsilon_z}\sin^2\alpha \pm \sqrt{D}$$

$$D=\frac{1}{\varepsilon_x^2}(\cos^2\alpha+\sin^2\alpha\sin^2\beta)^2 +\frac{1}{\varepsilon_y^2}(1-\sin^2\alpha\sin^2\beta)^2+\frac{1}{\varepsilon_z^2}\sin^4\alpha +\frac{2}{\varepsilon_x\varepsilon_y}(-\cos^2\alpha+\sin^4\alpha\sin^2\beta\cos^2\beta) +\frac{2}{\varepsilon_y\varepsilon_z}\sin^2\alpha(-\cos^2\beta+\sin^2\beta\cos^2\alpha) +\frac{2}{\varepsilon_z\varepsilon_x}\sin^2\alpha(-\sin^2\beta+\cos^2\alpha\cos^2\beta) \quad (26)$$

When $\beta = 0$ or π, the above solutions are simplified as given by Hesse et al.:

$$\varepsilon_1(\alpha,\omega)=\varepsilon_y(\omega) \quad (27)$$

$$\frac{1}{\varepsilon_2(\alpha,\omega)}=\frac{1}{\varepsilon_z(\omega)}\sin^2\alpha+\frac{1}{\varepsilon_x(\omega)}\cos^2\alpha. \quad (28)$$

If we use the model function given in Eqs. 23 and 24, $\varepsilon_2(\alpha,\omega)$ is given by the following Lorentz function:

$$\varepsilon_2(\alpha,\omega)=E(\alpha)+\frac{\Omega_p^2(\alpha)}{\Omega_0^2-\omega^2-i\gamma_x\omega} \quad (29)$$

where:

$$E(\alpha)=\frac{\varepsilon_z^0\varepsilon_x^0}{\varepsilon_z^0\cos^2\alpha+\varepsilon_x^0\sin^2\alpha} \quad (30)$$

$$\Omega_0(\alpha)=\frac{\omega_{px}}{\sqrt{\varepsilon_z^0\cos^2\alpha+\varepsilon_x^0\sin^2\alpha}} \quad (31)$$

$$\Omega_p(\alpha)=\frac{\varepsilon_z^0\omega_{px}}{\varepsilon_z^0\cos^2\alpha+\varepsilon_x^0\sin^2\alpha}. \quad (32)$$

When $\alpha = \pi/2$, in the case of the longitudinal excitation, the resonance energy of this Lorentz function is reduced to be $\Omega_0(\pi/2)=\frac{\omega_{px}}{\sqrt{\varepsilon_x^0}}$. Meanwhile the plasmon is detected by EELS, in which the excitation energy is given by the resonance energy of the function, $Im(-1/\varepsilon_x(\omega))$, which again provides us $\frac{\omega_{px}}{\sqrt{\varepsilon_x^0}}$. In the anisotropic medium, as shown in Eq. 31, the plasmon resonance energy depends upon the direction of the wavevector of the probe light.

Let us apply Eq. 26 to the $BO_2Cl(H_2O)_3$ crystal. We first fit the reflectivity curves (not shown) by the Drude model, and then adopt the Drude parameters of the dielectric functions for x and y directions (Eqs. 22 and 23) as $\varepsilon_x^0 = 3.10$, $\omega_{px} = 9980\ cm^{-1}$, $\gamma_x = 1170\ cm^{-1}$; $\varepsilon_y = 3.04$. $\omega_{py} = 8880\ cm^{-1}$, $\gamma_y = 1070\ cm^{-1}$. $\varepsilon_z = 3.0$ is estimated from the average reflectivity $R \approx 0.07$ in the 2000—3000 cm^{-1} region of the $E\perp[1\bar{1}0]$-on-(110) spectrum. The angles of $\boldsymbol{k_0}$ perpendicular to the (111) and (11$\bar{1}$) planes are calculated from the unit cell parameters as $\alpha = 71.0°$, $\beta = 56.9°$ and $\alpha = 101.3°$, $\beta = 60.7°$, respectively. The principal values $\sigma_2(\omega) = \varepsilon_0\varepsilon_2(\omega)\omega$ for the (111) and (11$\bar{1}$) planes are displayed in the bottom panel of Fig. 20 along with the principal values $\sigma_x(\omega)$ and $\sigma_y(\omega)$. The agreement with the observed values is excellent. The slight differences of the peak positions are ascribable to the Drude parameters.

Furthermore, we applied this solution to another compound $(BO)_{2.4}I_3$, which is more anisotropic. The conducting sheet expands in the (001) plane.[60,68] Since the conducting sheet is separated from the next sheet by I_3^- anions, $(BO)_{2.4}I_3$ is regarded as a quasi-two-dimensional metal. The needle-like crystal has a large (001) crystal face elongated along the b-axis. The next developed ($\bar{1}01$) face makes an angle of 67.0° with the (001) plane. The crystal face (010) is relatively large but the surface is not flat enough to do the reflectivity measurement. The reflectivity measured on the (001) face rotating the polarization direction results in the maximum reflectivity for $E//a$ and minimum reflectivity for $E\perp a$ in the IR region. Since the conducting sheet is parallel to this plane, the principal axes in the IR region is the directions of $//a$, $\perp a$ on (001) (defined as b' nearly parallel to b), and c^*, where c^* is the reciprocal axis perpendicular to (001) plane. The top panel of Fig. 22 shows the optical conductivity measured in three polarization directions. As shown in this figure, a similar band is observed more strongly on the ($\bar{1}01$) face of the crystal than for $BO_2Cl(H_2O)_3$.[62] As we expected, the intra-band absorption is found in the $E//a$ and $E\perp a$ spectra. We estimate the plasma frequency in both spectra using Eq. 13 and Hagen–Rubens extrapolation for $\sigma(\omega)$ below 600 cm^{-1}. The plasma frequencies thus obtained are respectively 8400 and 6000 cm^{-1} for $E//a$ and $E\perp a$ on (001) plane.

Let us apply Eq. 26 to $(BO)_{2.4}I_3$ crystal. We adopt the parameters of the dielectric functions for x, y, and z directions as $\varepsilon_x^0 = 3.0$, $\omega_{px} = 8400\ cm^{-1}$, $\gamma_x = 1500\ cm^{-1}$; $\varepsilon_y = 5.0$. $\omega_{py} = 6000\ cm^{-1}$, $\gamma_y = 1500\ cm^{-1}$; $\varepsilon_z = 4.0$. The angles of $\boldsymbol{k_0}$ for ($\bar{1}01$) direction are calculated from the unit cell parameters as $\alpha = 67.0°$ and $\beta = 172°$. The principal values $\sigma_1(\omega)$ and $\sigma_2(\omega)$ on the ($\bar{1}01$) plane are displayed in the bottom panel of Fig. 22 along with the principal values $\sigma_x(\omega)$ and $\sigma_y(\omega)$. The agreement with the observed spectrum is excellent.

6. Summary

The optical transition based on the one-electron theory is formulated for the one-dimensional system with a zigzag stack. The theoretical model predicts two optical transitions: the Drude-like absorption along the stacking direction and another one along the direction of zigzag. The former transition occurs mainly at the zone boundary ($k = \pi/c$), and the latter at the zone center ($k = 0$) between the folded bands. These two optical transitions are observed in the polarized reflection spectrum of DMTSA–BF_4. This theoretical model explains very well the spectral change caused by the phase transition. In section 2-3, the estimation of the transfer integrals is conducted in the quasi-two-dimensional system $(BDT\text{–}TTP)_2SbF_6$. The numerical calculation of the plasma frequency in the two-dimensional system provides us the estimation of the transfer integrals in two directions. Such an analysis reveals that the conventional calculation overestimates the inter-chain transfer integral by almost two times. The band structure of $(BDT\text{–}TTP)_2SbF_6$ is more two-dimensional than that of Bechgaard salts which have the band structure similar to this compound.

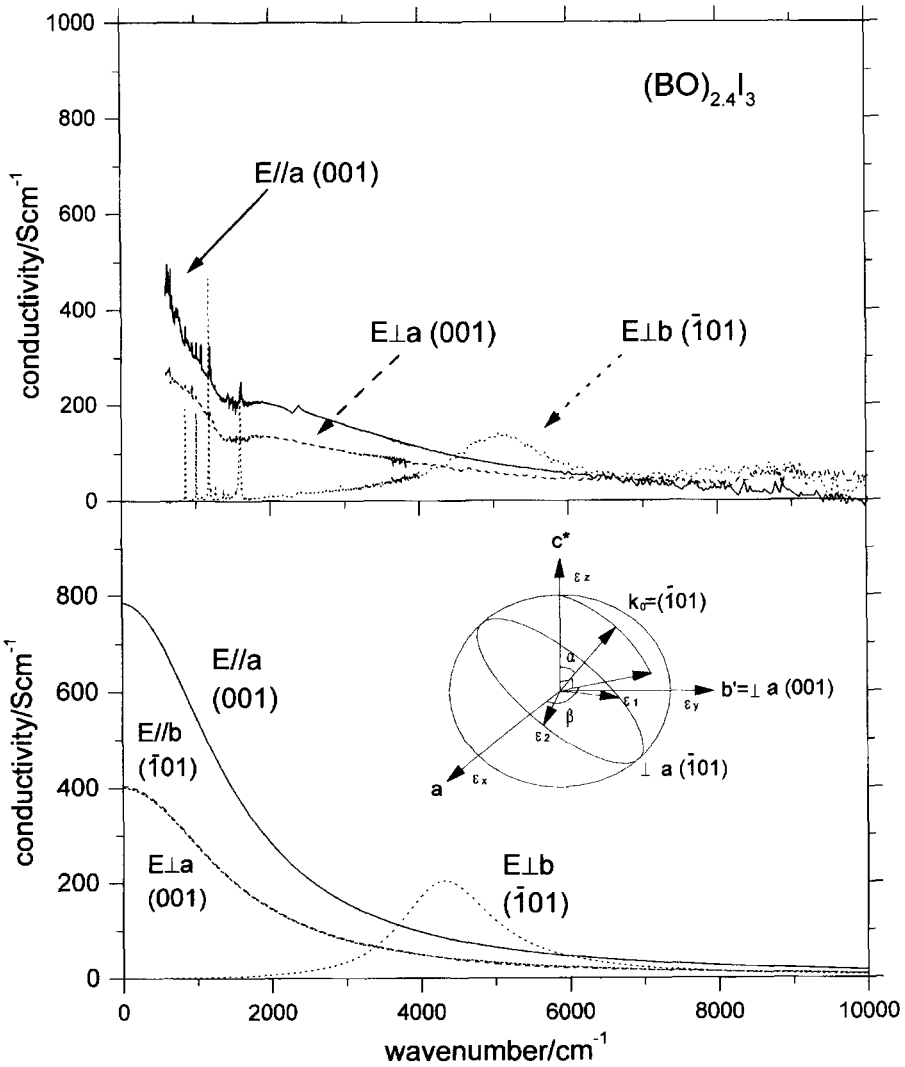

Fig. 22. Observed and calculated optical conductivity of $(BO)_{2.4}I_3$. Plasmon is observed as well as $(BO)_2Cl(H_2O)_3$. See Figs. 20 and 21.

The electron–electron interaction gives the charge carriers a localized nature, and it makes the optical transition very different from the simple Drude model. The theoretical description of the optical transition based on the half-filled one-dimensional Hubbard model is applied to the experimental observation in DMTTA–BF_4 in section 3-1. (BEDT–ATD)$_2PF_6$(DHF) is regarded as the strongly correlated quarter-filled quasi-one-dimensional system. The unusual line shape of the lowest excitation in this compound is discussed from the viewpoint of strong correlation.

The dimer model for the vibronic bands is successfully applied to DMTSA–ClO_4. The interaction with molecular vibrations in this molecule is characterized. The vibronic band is used as an indicator to demonstrate the breaking of the symmetry in the infinite chain system. It is applied to detect the symmetry breaking during the phase transition utilizing the high sensitivity to the local symmetry breaking. In section 4-2, the appearance of the vibronic bands in (BEDT–ATD)$_2PF_6$(DHF), DMTSF–BF_4, and DMTTA–BF_4, are compared with the violation of the extinction rule in x-ray diffraction. In the case of BEDT–ATD salt, the x-ray diffraction corresponds very well with the optical experiment. However, the x-ray experiment cannot detect the breaking of the symmetry predicted by the optical experiment. The latter may show the difference in sensitivity. Section 4-3 describes the vibronic band in the quasi-two-dimensional system. The selection rule for vibronic mode is expanded by taking the inter-stack charge-transfer interaction into account.

The longitudinal excitation cannot be detected by the optical reflectivity in an isotropic material. However, it can be detected in an anisotropic material, since the longitudinal and transverse excitations mix with each other when the reflectivity measurement is conducted in some directions not parallel to the optical axis. The plasmon was first observed by normal incidence reflectivity in quasi-two-dimensional organic conductors $(BO)_2Cl(H_2O)_3$ and $(BO)_{2.4}I_3$. A general formula is derived from the Fresnel equation.

The results introduced in this article have been performed with many collaborators. The spectroscopic studies on the charge-transfer salts of DMTSA, DMTTA, and BDT–TTP

were taken from the Ph. D. Thesis of Dr. J. Ouyang of the Graduate University for Advanced Studies. Prof. T. Otsubo and Dr. K. Takimiya of Hiroshima University provides us DMTSA and DMTTA molecules, and Drs. J. Dong and C. Nakano of IMS grew the nice single crystals of DMTSA and DMTTA charge-transfer salts. Profs. Y. Misaki and K. Tanaka of Kyoto University provided us the high quality of single crystals of various BDT-TTP charge-transfer salts. The spectroscopic study of (BEDT–ATD)$_2$PF$_6$(DHF) is part of in the Ph. D. Thesis which Mr. M. Uruichi has submitted to the Graduate University for Advanced Studies. Prof. Y. Yamashita kindly supplied all the single crystals of (BEDT–ATD)$_2$X(solvent) system. Prof. J. Ulanski of Technical University of Lodz (Poland) has done the observation of the plasmon in two-dimensional metal BEDO-TTF salts, when he stayed in IMS as a visiting professor. Profs. G. Saito and H. Yamochi provided us large single crystals of BEDO–TTF salts with a high quality. The author wishes to express his hearty thanks to all of them for their kind collaborations. The author is indebted to Mrs. Y. Horigome, K. Suzui, N. Mizutani, K. Kobayashi, H. Yoshida, T. Toyoda, and K. Uchiyama of the Equipment Development Center in IMS for their assistance during setting up and improving the micro-spectrometer and Raman spectrometer. This research was partly supported by a Grant-in-Aid for Scientific Research on Priority Areas (B) of Molecular Conductors and Magnets (Area No. 730/Grant No.11224212) from the Ministry of Education, Science, Sports, and Culture.

References

1 H. Basista, D. A. Bonn, T. Timusk, J. Voit, D. Jerome, and K. Bechgaard, *Phys. Rev. B*, **42**, 4088 (1990).

2 V. Vescoli, L. Degiorgi, W. Henderson, G. Gruner, K. P. Starkey, and L. K. Montgomery, *Science*, **281**, 1181 (1998).

3 N. Cao, T. Timusk, and K. Bechgaard, *J. Phys. I France*, **6**, 1719 (1996).

4 J. Wosnitza, "Fermi surfaces of low-dimensional organic metals and superconductors," Springer, Berlin (1996).

5 I. A. Musurkin and A. A. Ovchinnikov, *Soviet Physics Solid State*, **12**, 2031, (1971).

6 D. Baeriswyl, J. Carmelo, and A. Luther, *Phys. Rev. B*, **33**, 7247, (1986).

7 J. Favand and F. Mila, *Phys. Rev. B*, **54**, 10425 (1996).

8 M. J. Rice, V. M. Yartsev, and C. S. Jacobsene, *Phys. Rev. B*, **21**, 3437, (1980).

9 T. Ishiguro and K. Yamaji, "Organic Superconductors, Springer Series in Solid-State Science," **88**, (1989), p. 187.

10 M. J. Rice, *Solid State Commun.*, **31**, 93 (1979).

11 R. Bozio, M. Meneghetti, and C. Pecile, *Phys. Rev. B*, **36**, 7795 (1987).

12 H. J. Hesse, W. Fuhs, G. Weiser, and L. von Szentpaly, *Phys. Status. Solidi B*, **76**, 817 (1976).

13 J. Dong, K. Yakushi, and Y. Yamashita, *J. Mater. Chem.*, **5**, 1735 (1995).

14 R. K. Ahrenkiel, *J. Opt. Soc. Am.*, **61**, 1651 (1971).

15 J. Ouyang, K. Yakushi, K. Takimiya, T. Otsubo, and H. Tajima, *Solid State Commun.*, **110**, 63 (1999).

16 J. Ouyang, J. Dong, K. Yakushi, K. Takimiya, and T. Otsubo, *J. Phys. Soc. Jpn.*, **68**, 3708 (1999).

17 J. Dong, K. Yakushi, Y. Yamashita, K. Imaeda, and H. Inokuchi, *Phys. Status. Solidi B*, **195**, 611 (1996).

18 K. Takimiya, A. Ohnishi, Y. Aso, T. Otsubo, F. Ogura, K. Kawabata, K. Tanaka, and M. Mizutani, *Bull. Chem. Soc. Jpn.*, **67**, 766 (1994).

19 V. Heine, "Group Theory in Quantum Mechanics," Pergamon, Oxford (1960), p. 284.

20 M. Tamura, Thesis, University of Tokyo, 1994.

21 H. Tajima, K. Yakushi, and H. Kuroda, *Solid State Commun.*, **56**, 159 (1985); H. Kuroda, K. Yakushi, H. Tajima, A. Ugawa, M. Tamura, Y. Okawa, A. Kobayashi, R. Kato, H. Kobayashi, and G. Saito, *Synth. Met.*, **27**, A 491 (1988).

22 H. Tajima, K. Yakushi, and H. Kuroda, *Solid State Commun.*, **56**, 251 (1985).

23 H. Kuroda, K. Yakushi, and H. Tajima, *Mol. Cryst. Liq. Cryst.*, **125**, 135 (1985).

24 J. B. Torrance, B. A. Scott, B. Welber, F. B. Kaufman, and P. E. Seiden, *Phys. Rev. B*, **19**, 730 (1979).

25 C. S. Jacobsene, D. B. Tanner, and K. Bechgaard, *Phys. Rev. B*, **28**, 7019 (1983).

26 J. Ouyang, K. Yakushi, Y. Misaki, and K. Tanaka, *J. Phys. Soc. Jpn.*, **67**, 3191 (1998).

27 The vibronic structure is ascribed to the electron-molecular coupling as will be discussed in section 4.

28 H. Tajima, Ph. D. Thesis, University of Tokyo (1989).

29 Y. Misaki, H. Fujiwara, T. Yamabe, T. Mori, H. Mori, and S. Tanaka, *Chem. Lett.*, **1653**, (1994).

30 T. Mori, Y. Misaki, H. Fujiwara, and T. Yamabe, *Bull. Chem. Soc. Jpn.*, **67**, 2685 (1994).

31 N. Thorup, G. Rindorf, H. Soling, and K. Bechgaard, *Acta Crystallogr. Sect B*, **37**, 1236 (1981).

32 C. S. Jacobsen, J. M. Williams, and H. H. Wang, *Solid State Commun.*, **54**, 937 (1985).

33 C. S. Jacobsen, D. B. Tanner, and K. Bechgaard, *Phys. Rev. B*, **28**, 7019 (1983).

34 J. Ouyang, Thesis, Graduate University for Advanced Studies (1999).

35 L. Ducasse, M. Abderrabba, J. Hoarau, M. Pesquer, B. Gallois, and J. Gaultier, *J. Phys. C: Solid State Phys.*, **19**, 3805 (1986).

36 M. Uruichi, K. Yakushi, and Y. Yamashita, *J. Phys. Soc. Jpn.*, **68**, 531 (1999).

37 M. Uruichi, K. Yakushi, and Y. Yamashita, *J. Mater. Chem.*, in press.

38 Y. Yamashita, S. Tomura, and K. Imaeda, *Synth. Met.*, **71**, 1965 (1995).

39 Y. Yamashita, M. Tomura, S. Tanaka, and K. Imaeda, *Synth. Met.*, **86**, 1795 (1997).

40 K. Imaeda, Y. Yamashita, S. Tanaka, and H. Inokuchi, *Mol. Cryst. Liq. Cryst.*, **296**, 205 (1997).

41 H. Tajima, K. Yakushi, and H. Kuroda, *Solid State Commun.*, **56**, 159 (1985).

42 C. S. Jacobsen, Ib Johannsen, and K. Bechgaard, *Phys. Rev. Lett.*, **53**, 194 (1984).

43 T. Giamarchi, *Physica B*, **230-232**, 975 (1997).

44 The charge separation is actually observed in the Raman spectrum of (BEDT–ATD)$_2$PF$_6$(THF) at low temperature, and the fluctuation is found already at room temperature as well (See Ref. 36).

45 The origin of this broad dip cannot be understood based on the conventional electron-molecular-vibration (emv) coupling

theory, since the temperature dependence of this dip is very different from other sharp vibronic bands as will be shown in section 4-2.

46 H. Tajima, *Solid State Commun.*, **113**, 279 (2000).

47 The decoupled modes are Raman and infrared active in this moleocule, since DMTSA does not have center of symmetry.

48 M. J. Rice, N. O. Lipari, and S. Strassler, *Phys. Rev. Lett.*, **39**, 1359 (1977).

49 A. Painelli and A. Girlando, *J. Chem. Phys.*, **84**, 5655 (1986).

50 This geometrical change is reproduced by the geometrical optimization of PM3 molecular orbital calculation.

51 R. Bozio, A. Cirlando, and C. Pecile, *J. Chem. Soc., Faraday Trans. 2*, **71**, 1237 (1975).

52 M. E. Kozlov, K. I. Pokhondnia, and A. A. Yurchenko, *Spectrochim. Acta Part A*, **45A**, 437 (1989).

53 J. Dong, K. Yakushi, K. Takimiya, and T. Otsubo, *J. Phys. Soc. Jpn.*, **67**, 3191 (1998).

54 T. Kambe, N. Fujimura, Y. Nogami, K. Oshima, K. Yakushi, J. Dong, K. Takimiya, and T. Otsubo, *Synth. Met.*, to be published.

55 This band can be assigned to the infrared-active ν_{22} (b_{1u}) mode as well.

56 J. Ouyang, K. Yakushi, T. Kinoshita, N. Nambu, M. Aoyagi, Y. Misaki, and K. Tanaka, *Spectrochim. Acta Part A*, in preparation.

57 M. Taniguchi, Y. Misaki, and K. Tanaka, *Solid State Commun.*, **114**, 75 (2000).

58 M. D. Sturge, H. J. Guggenheim, and M. H. L. Pryce, *Phys. Rev. B*, **2** (1970) 2459.

59 K. Yakushi, J. Ulanski, H. Yamochi, and G. Saito, *Phys. Rev. B*, **61**, 9891 (2000-I).

60 F. Wudl, H. Yamochi, T. Suzuki, H. Isotalo, C. Fite, H. Kasmai, K. Liou, G. Srdanov, P. Coppens, K. Maly, and A. Frost-Jensen, *J. Am. Chem. Soc.*, **112**, 2461 (1990).

61 H. Yamochi, T. Nakamura, G. Saito, T. Sugano, and F. Wudl, *Synth. Met.*, **42**, 1741 (1991).

62 J. Ulanski, K. Yakushi, M. Uruichi, O. Drozdova, H. Yamochi, and G. Saito, *J. Phys.C: Condensed Matter*, in preparation.

63 D. Schweitzer, S. Kahlich, I. Heinen, Son-En Lan, B. Nuber, H. Keller, K. Winzer, and H. W. Helberg, *Synth. Met.*, **56**, 2827 (1993).

64 T. Mori, S. Ono, H. Mori, and S. Tanaka, *J. Phys. I*, **6**, 1849 (1996).

65 T. Mori, K. Oshima, H. Okuno, K. Kato, H. Mori, and S. Tanaka, *Phys. Rev. B*, **51**, 11110 (1995-II).

66 M. A. Tanatar, R. Swietlik, N. D. Kushch, and E. B. Yagugskii, *J. Phys. C: Condens. Matter*, **9**, 6383 (1997).

67 This is assigned to the electronic transition from the second HOMO to HOMO in BO^+ cation radical. S. Horiuchi, H. Yamochi, G. Saito, J. K. Jeszka, A. Tracz, A. Sroczynska, and J. Ulanski, *Mol. Cryst. Liq. Cryst.*, **296**, 365 (1997).

68 H. Yamochi, T. Nakamura, G. Saito, T. Sugano, and F. Wudl, *Synth. Met.*, **42**, 1741 (1991).

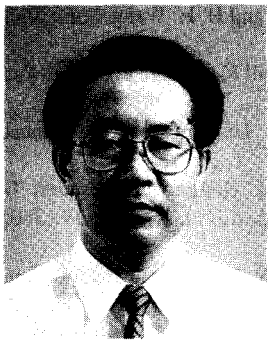

Kyuya Yakushi was born in 1945 in Kagoshima, Japan. He received his B. Sc. in 1968 and M. Sc. in 1970 from the University of Tokyo. He was appointed to be a research associate of the Department of Chemistry of the University of Tokyo in 1972. He earned his Ph. D. from the University of Tokyo in 1976 on the crystal structure of charge-transfer compounds. He experienced a post-doctoral position in IBM San Jose Laboratory for the spectroscopic study of a conducting polymer during 1982—1983. He was appointed as an associate professor of the University of Tokyo in 1985. Since 1988 he has been the full professor of Institute for Molecular Science at Okazaki. His research interest in the study of organic conductors utilizing reflection and Raman spectroscopy.